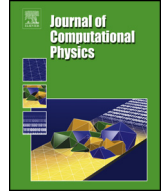




Contents lists available at ScienceDirect

Journal of Computational Physics

www.elsevier.com/locate/jcp


Local characteristic decomposition based central-upwind scheme

Alina Chertock^a, Shaoshuai Chu^{b,*}, Michael Herty^c, Alexander Kurganov^d,
Mária Lukáčová-Medvid'ová^e

^a Department of Mathematics, North Carolina State University, Raleigh, NC 27695, USA

^b Department of Mathematics, Southern University of Science and Technology, Shenzhen, 518055, China

^c Department of Mathematics, RWTH Aachen University, 52056 Aachen, Germany

^d Department of Mathematics, SUSTech International Center for Mathematics and Guangdong Provincial Key Laboratory of Computational Science and Material Design, Southern University of Science and Technology, Shenzhen, 518055, China

^e Institute of Mathematics, University of Mainz, Germany

ARTICLE INFO

Article history:

Received 16 June 2022

Received in revised form 8 October 2022

Accepted 16 October 2022

Available online 24 October 2022

Keywords:

Local characteristic decomposition

Central-upwind schemes

Hyperbolic systems of conservative laws

Euler equations of gas dynamics

ABSTRACT

We propose novel less diffusive schemes for conservative one- and two-dimensional hyperbolic systems of nonlinear partial differential equations (PDEs). The main challenges in the development of accurate and robust numerical methods for the studied systems come from the complicated wave structures, such as shocks, rarefactions and contact discontinuities, arising even for smooth initial conditions. In order to reduce the diffusion in the original central-upwind schemes, we use a local characteristic decomposition procedure to develop a new class of central-upwind schemes. We apply the developed schemes to the one- and two-dimensional Euler equations of gas dynamics to illustrate the performance on a variety of examples. The obtained numerical results clearly demonstrate that the proposed new schemes outperform the original central-upwind schemes.

© 2022 Elsevier Inc. All rights reserved.

1. Introduction

This paper focuses on numerical solutions of hyperbolic systems of conservation laws, which in the two-dimensional (2-D) case, read as

$$\mathbf{U}_t + \mathbf{F}(\mathbf{U})_x + \mathbf{G}(\mathbf{U})_y = \mathbf{0}, \quad (1.1)$$

where x and y are spatial variables, t is the time, $\mathbf{U} \in \mathbb{R}^d$ is a vector of unknowns, $\mathbf{F} : \mathbb{R}^d \rightarrow \mathbb{R}^d$ and $\mathbf{G} : \mathbb{R}^d \rightarrow \mathbb{R}^d$ are the x - and y -flux functions, respectively.

It is well-known that the solutions of (1.1) may develop complicated wave structures including shocks, rarefactions, and contact discontinuities even for infinitely smooth initial data, and thus developing highly accurate and robust shock-capturing numerical methods for solving (1.1) is a challenging task.

Since the pioneering works [7,9,24], a large number of various methods had been introduced; see, e.g., the monographs and review papers [2,12,16,25,39,42] and references therein. Here, we focus on finite-volume (FV) methods, in which solu-

* Corresponding author.

E-mail addresses: chertock@math.ncsu.edu (A. Chertock), chuss2019@mail.sustech.edu.cn (S. Chu), herty@mathc.rwth-aachen.de (M. Herty), alexander@sustech.edu.cn (A. Kurganov), lukacova@uni-mainz.de (M. Lukáčová-Medvid'ová).

tions are realized in terms of their cell averages and evolved in time according to the following algorithm. First, a piecewise polynomial interpolant is reconstructed out of the given cell averages, and then the evolution step is performed using the integral form of (1.1). To this end, a proper set of time-space control volumes has to be selected. Depending on this selection, one may distinguish between two basic classes of finite-volume methods: upwind and central schemes. In upwind schemes, the spatial part of the control volumes coincides with the FV cells and therefore, one needs to (approximately) solve (generalized) Riemann problems at every cell interface; see, e.g., [2,9,42] and references therein. This helps the upwind schemes to achieve very high resolution. At the same time, it might be quite complicated and even impossible to solve the (generalized) Riemann problems for general systems of conservation laws. Central schemes offer an attractive simple alternative to the upwind ones. In staggered central schemes, first proposed for one-dimensional (1-D) systems in [32] and then extended to higher order [26,31] and multiple number of dimensions [1,13,27], the control volumes use the staggered spatial parts so that the FV cell interfaces remain inside the control volumes. This allows to avoid even approximately solving any Riemann problems, which makes staggered central schemes easy to implement for a wide variety of hyperbolic systems. The major drawback of staggered central schemes is, however, their relatively large numerical dissipation as they basically average over the Riemann fans rather than resolving them.

In order to reduce the amount of excessive numerical dissipation present in central schemes, a class of central-upwind (CU) schemes have been proposed in [18,21]. These schemes are based on nonuniform control volumes, whose spatial size taken to be proportional to the local speeds of propagation. This allows one to minimize the area over which the solution averaging occurs still without (approximately) solving any (generalized) Riemann problems. The upwind features of the CU schemes can be seen, for example, when they are applied to simpler systems. For instance, the CU scheme from [18] reduces to the upwind one when it is applied to a system whose Jacobian contains only positive (only negative) eigenvalues. Another advantage of the CU schemes is related to the fact that unlike the staggered central schemes, they admit a particularly simple semi-discrete form. This observation is the basis of the modifications of the CU schemes we propose in this paper.

Even though the CU schemes from [18,21] are quite accurate, efficient and robust tools for a wide variety of hyperbolic systems, higher resolution of the numerical solutions can be achieved by further reducing numerical dissipation. This can be done in a number of different ways, for example: (i) by introducing a more accurate evolution procedure, which leads to a “built-in” anti-diffusion term [20]; (ii) by implementing a numerical dissipation switch to control the amount of numerical dissipation present in the CU schemes [17]; (iii) by obtaining more accurate estimates for the one-sided local speeds of propagation using the discrete Rankine-Hugoniot conditions [8].

Another way to control the amount of numerical dissipation present in the CU schemes or any other FV methods is by adjusting the nonlinear limiting mechanism used in the piecewise polynomial reconstruction. It is well-known that sharper reconstructions may lead to larger numerical oscillations and a way to reduce these oscillations is to reconstruct the characteristic variables rather than the conservative ones; see, e.g., [35]. This can be done using the local characteristic decomposition (LCD); see, e.g., [3,14,15,30,33,35,39,44] and references therein.

In this paper, we modify the CU schemes from [18] by applying LCD to the numerical diffusion part of the schemes. The obtained new LCD-based CU schemes contain substantially smaller amount of numerical dissipation, which leads to a significantly improved resolution of the computed solution compared with the original CU schemes. As observed above, the key idea is that the new LCD-based CU scheme reduces to the upwind scheme when applied to 1-D linear hyperbolic systems

$$\mathbf{U}_t + A\mathbf{U}_x = \mathbf{0}, \tag{1.2}$$

where A is a constant matrix (disregarding the sign of the eigenvalues of A). This feature suggests that the new CU schemes have more built-in upwinding compared with their predecessors.

The paper is organized as follows. In §2, we briefly describe the 1-D second-order FV CU scheme from [18]. In §3, we introduce the proposed new 1-D LCD-based CU scheme and show that the developed 1-D scheme reduces to the upwind scheme when applied to the linear system (1.2). In §4, we construct the 2-D LCD-based CU scheme. Finally, in §5, we test the proposed schemes on a number of 1-D and 2-D numerical examples for the Euler equations of gas dynamics. We demonstrate high accuracy, efficiency, stability, and robustness of the new LCD-based CU schemes, which clearly outperform the second-order CU scheme from [18,22].

2. 1-D central-upwind scheme: a brief overview

In this section, we consider the 1-D hyperbolic system of conservation laws

$$\mathbf{U}_t + \mathbf{F}(\mathbf{U})_x = \mathbf{0}, \tag{2.1}$$

and describe the second-order semi-discrete CU scheme from [18]. To this end, we assume that the computational domain is covered with the uniform cells $C_j := [x_{j-\frac{1}{2}}, x_{j+\frac{1}{2}}]$ of size Δx centered at $x_j = (x_{j-\frac{1}{2}} + x_{j+\frac{1}{2}})/2$ and denote by $\bar{\mathbf{U}}_j(t)$ cell averages of $\mathbf{U}(\cdot, t)$ over the corresponding intervals C_j , that is,

$$\bar{\mathbf{U}}_j(t) \approx \frac{1}{\Delta x} \int_{C_j} \mathbf{U}(x, t) dx.$$

We also assume that at certain time $t \geq 0$, the cell average values $\bar{\mathbf{U}}_j$ are available and from here on we suppress the time-dependence of all of the indexed quantities for the sake of brevity.

According to [18], the computed cell averages (2.1) are evolved in time by solving the following system of ordinary differential equations (ODEs):

$$\frac{d\bar{\mathbf{U}}_j}{dt} = -\frac{\mathcal{F}_{j+\frac{1}{2}} - \mathcal{F}_{j-\frac{1}{2}}}{\Delta x}, \tag{2.2}$$

where $\mathcal{F}_{j+\frac{1}{2}}$ are the CU numerical fluxes given by

$$\mathcal{F}_{j+\frac{1}{2}} = \frac{a_{j+\frac{1}{2}}^+ \mathbf{F}_{j+\frac{1}{2}}^- - a_{j+\frac{1}{2}}^- \mathbf{F}_{j+\frac{1}{2}}^+}{a_{j+\frac{1}{2}}^+ - a_{j+\frac{1}{2}}^-} + \frac{a_{j+\frac{1}{2}}^+ a_{j+\frac{1}{2}}^-}{a_{j+\frac{1}{2}}^+ - a_{j+\frac{1}{2}}^-} \left(\mathbf{U}_{j+\frac{1}{2}}^+ - \mathbf{U}_{j+\frac{1}{2}}^- \right). \tag{2.3}$$

Here, $\mathbf{F}_{j+\frac{1}{2}}^\pm := \mathbf{F}(\mathbf{U}_{j+\frac{1}{2}}^\pm)$ and $\mathbf{U}_{j+\frac{1}{2}}^\pm$ are the right/left-sided values reconstructed out of the given set of cell averages $\{\bar{\mathbf{U}}_j\}$. The one-sided local speeds of propagation $a_{j+\frac{1}{2}}^\pm$ are estimated using the largest and the smallest eigenvalues of the Jacobian $A(\mathbf{U}) := \frac{\partial \mathbf{F}}{\partial \mathbf{U}}(\mathbf{U})$, which we denote by $\lambda_1(A(\mathbf{U})) \leq \dots \leq \lambda_d(A(\mathbf{U}))$. This can be done, for example, by taking

$$\begin{aligned} a_{j+\frac{1}{2}}^+ &= \max \left\{ \lambda_d(A(\mathbf{U}_{j+\frac{1}{2}}^+)), \lambda_d(A(\mathbf{U}_{j+\frac{1}{2}}^-)), 0 \right\}, \\ a_{j+\frac{1}{2}}^- &= \min \left\{ \lambda_1(A(\mathbf{U}_{j+\frac{1}{2}}^+)), \lambda_1(A(\mathbf{U}_{j+\frac{1}{2}}^-)), 0 \right\}. \end{aligned} \tag{2.4}$$

The (formal) order of the scheme (2.2)–(2.4) is determined by the accuracy the point values $\mathbf{U}_{j+\frac{1}{2}}^\pm$ are reconstructed with and the order of the ODE solver used to integrate the ODE system (2.2) in time. In this paper, we use the LCD-based second-order piecewise linear reconstruction described in §2.1 and the three-stage third-order strong stability preserving (SSP) Runge-Kutta solver; see, e.g., [10,11].

2.1. LCD-based piecewise linear reconstruction

In order to ensure at least second-order of accuracy of the CU scheme (2.2)–(2.4), one has to use a second-order piecewise linear reconstruction, which will be non-oscillatory provided the numerical derivatives are computed using a nonlinear limiter. A library of different limiters are available; see, e.g., [2,12,25,28,32,41,42]. The limiters can be classified as dissipative, compressive or overcompressive; see [28]. When applied to the conservative variables \mathbf{U} , dissipative limiters may introduce excessive numerical dissipation, which may result in oversmeared solution discontinuities. On the other hand, compressive and overcompressive limiters tend to lead to quite large oscillations near discontinuities and artificial sharpening smooth parts of the solution (compressive limiters may lead to kinks, that is, jumps in the first derivatives, while the overcompressive limiters may lead to jumps in the solution itself); see, e.g., [28]. Part of these difficulties can be overcome by reconstructing local characteristic variables as it was demonstrated in [35] in the context of higher-order WENO reconstructions.

In this paper, we use the minmod limiter, which is, according to [28], the most compressive out of dissipative limiters. As this limiter typically leads to quite large oscillations when applied to the conservative variables, we implement it in the LCD framework. Specifically, we first introduce the matrix $\hat{A}_{j+\frac{1}{2}} = A(\hat{\mathbf{U}}_{j+\frac{1}{2}})$, where $A(\mathbf{U}) = \frac{\partial \mathbf{F}}{\partial \mathbf{U}}(\mathbf{U})$ is the Jacobian and $\hat{\mathbf{U}}_{j+\frac{1}{2}}$ is either a simple average $(\bar{\mathbf{U}}_j + \bar{\mathbf{U}}_{j+1})/2$ or another type of average of the $\bar{\mathbf{U}}_j$ and $\bar{\mathbf{U}}_{j+1}$ states.

As long as the system (1.1) is strictly hyperbolic, we compute the matrices $R_{j+\frac{1}{2}}$ and $R_{j+\frac{1}{2}}^{-1}$ such that $R_{j+\frac{1}{2}}^{-1} \hat{A}_{j+\frac{1}{2}} R_{j+\frac{1}{2}}$ is a diagonal matrix and introduce the local characteristic variables Γ_k in the neighborhood of $x = x_{j+\frac{1}{2}}$:

$$\Gamma_k = R_{j+\frac{1}{2}}^{-1} \bar{\mathbf{U}}_k, \quad k = j - 1, \dots, j + 2.$$

Equipped with the values Γ_{j-1} , Γ_j , Γ_{j+1} and Γ_{j+2} , we reconstruct Γ in the cell C_j by computing

$$(\Gamma_x)_j = \text{minmod} \left(2 \frac{\Gamma_j - \Gamma_{j-1}}{\Delta x}, \frac{\Gamma_{j+1} - \Gamma_{j-1}}{2\Delta x}, 2 \frac{\Gamma_{j+1} - \Gamma_j}{\Delta x} \right), \tag{2.5}$$

and

$$(\Gamma_x)_{j+1} = \text{minmod} \left(2 \frac{\Gamma_{j+1} - \Gamma_j}{\Delta x}, \frac{\Gamma_{j+2} - \Gamma_j}{2\Delta x}, 2 \frac{\Gamma_{j+2} - \Gamma_{j+1}}{\Delta x} \right), \tag{2.6}$$

where the minmod function, defined as

$$\text{minmod}(z_1, z_2, \dots) := \begin{cases} \min_j \{z_j\} & \text{if } z_j > 0 \quad \forall j, \\ \max_j \{z_j\} & \text{if } z_j < 0 \quad \forall j, \\ 0 & \text{otherwise,} \end{cases} \tag{2.7}$$

is applied in the component-wise manner. The slopes (2.5) and (2.6) allow to evaluate

$$\mathbf{\Gamma}_{j+\frac{1}{2}}^- = \mathbf{\Gamma}_j + \frac{\Delta x}{2}(\mathbf{\Gamma}_x)_j \quad \text{and} \quad \mathbf{\Gamma}_{j+\frac{1}{2}}^+ = \mathbf{\Gamma}_{j+1} - \frac{\Delta x}{2}(\mathbf{\Gamma}_x)_{j+1},$$

and obtain the corresponding point values of \mathbf{U} by

$$\mathbf{U}_{j+\frac{1}{2}}^\pm = R_{j+\frac{1}{2}} \mathbf{\Gamma}_{j+\frac{1}{2}}^\pm. \tag{2.8}$$

Remark 2.1. In Appendix A, we provide a detailed explanation on how the average matrix $\widehat{A}_{j+\frac{1}{2}}$ and the corresponding matrices $R_{j+\frac{1}{2}}$ and $R_{j+\frac{1}{2}}^{-1}$ are computed in the case of the Euler equation of gas dynamics.

3. 1-D LCD-based central-upwind scheme

In this section, we introduce a new 1-D LCD-based CU scheme, in which the amount of numerical dissipation is substantially reduced compared with the original CU scheme (2.2)–(2.3). To this end, we first rewrite the numerical flux (2.3) of the original CU scheme in the following form:

$$\mathcal{F}_{j+\frac{1}{2}} = \frac{\mathbf{F}_j + \mathbf{F}_{j+1}}{2} + \mathbf{D}_{j+\frac{1}{2}}, \tag{3.1}$$

where $\mathbf{F}_j := \mathbf{F}(\bar{\mathbf{U}}_j)$ and $\mathbf{D}_{j+\frac{1}{2}}$ is the numerical diffusion given by

$$\begin{aligned} \mathbf{D}_{j+\frac{1}{2}} &= \frac{a_{j+\frac{1}{2}}^+}{a_{j+\frac{1}{2}}^+ - a_{j+\frac{1}{2}}^-} \left[\mathbf{F}_{j+\frac{1}{2}}^- - \frac{\mathbf{F}_j + \mathbf{F}_{j+1}}{2} \right] - \frac{a_{j+\frac{1}{2}}^-}{a_{j+\frac{1}{2}}^+ - a_{j+\frac{1}{2}}^-} \left[\mathbf{F}_{j+\frac{1}{2}}^+ - \frac{\mathbf{F}_j + \mathbf{F}_{j+1}}{2} \right] \\ &\quad + \frac{a_{j+\frac{1}{2}}^+ a_{j+\frac{1}{2}}^-}{a_{j+\frac{1}{2}}^+ - a_{j+\frac{1}{2}}^-} \left(\mathbf{U}_{j+\frac{1}{2}}^+ - \mathbf{U}_{j+\frac{1}{2}}^- \right), \end{aligned}$$

which, in turn, can be rewritten with the help of the matrix $R_{j+\frac{1}{2}}$ introduced in §2.1 and using (2.8) as follows:

$$\begin{aligned} \mathbf{D}_{j+\frac{1}{2}} &= R_{j+\frac{1}{2}} P_{j+\frac{1}{2}} R_{j+\frac{1}{2}}^{-1} \left[\mathbf{F}_{j+\frac{1}{2}}^- - \frac{\mathbf{F}_j + \mathbf{F}_{j+1}}{2} \right] + R_{j+\frac{1}{2}} M_{j+\frac{1}{2}} R_{j+\frac{1}{2}}^{-1} \left[\mathbf{F}_{j+\frac{1}{2}}^+ - \frac{\mathbf{F}_j + \mathbf{F}_{j+1}}{2} \right] \\ &\quad + R_{j+\frac{1}{2}} Q_{j+\frac{1}{2}} \left(\mathbf{\Gamma}_{j+\frac{1}{2}}^+ - \mathbf{\Gamma}_{j+\frac{1}{2}}^- \right). \end{aligned} \tag{3.2}$$

Here, $P_{j+\frac{1}{2}}$, $M_{j+\frac{1}{2}}$, and $Q_{j+\frac{1}{2}}$ are the diagonal matrices

$$\begin{aligned} P_{j+\frac{1}{2}} &= \text{diag}((P_1)_{j+\frac{1}{2}}, \dots, (P_d)_{j+\frac{1}{2}}), \quad M_{j+\frac{1}{2}} = \text{diag}((M_1)_{j+\frac{1}{2}}, \dots, (M_d)_{j+\frac{1}{2}}), \\ Q_{j+\frac{1}{2}} &= \text{diag}((Q_1)_{j+\frac{1}{2}}, \dots, (Q_d)_{j+\frac{1}{2}}) \end{aligned} \tag{3.3}$$

with

$$((P_i)_{j+\frac{1}{2}}, (M_i)_{j+\frac{1}{2}}, (Q_i)_{j+\frac{1}{2}}) = \frac{1}{a_{j+\frac{1}{2}}^+ - a_{j+\frac{1}{2}}^-} (a_{j+\frac{1}{2}}^+, -a_{j+\frac{1}{2}}^-, a_{j+\frac{1}{2}}^+ a_{j+\frac{1}{2}}^-), \quad i = 1, \dots, d. \tag{3.4}$$

The main idea of the new the 1-D LCD-based CU scheme is to replace the constant entries (3.4) in the diagonal matrices $P_{j+\frac{1}{2}}$, $M_{j+\frac{1}{2}}$, and $Q_{j+\frac{1}{2}}$ with the corresponding characteristic entries of the diagonal matrix $R_{j+\frac{1}{2}}^{-1} \widehat{A}_{j+\frac{1}{2}} R_{j+\frac{1}{2}}$. This is motivated by the fact that in the linear case with $\mathbf{F}(\mathbf{U}) = \mathbf{A}\mathbf{U}$, the local characteristic speed might be different for each (diagonalized) component \mathbf{F} . Hence, a diffusion that depends on the corresponding local speed of each component may lead to a sharper resolution of possible discontinuities.

Proposed modifications lead to the semi-discrete scheme

$$\frac{d\bar{\mathbf{U}}_j}{dt} = - \frac{\mathcal{F}_{j+\frac{1}{2}}^{\text{LCD}} - \mathcal{F}_{j-\frac{1}{2}}^{\text{LCD}}}{\Delta x}, \tag{3.5}$$

where the numerical fluxes $\mathcal{F}_{j+\frac{1}{2}}^{\text{LCD}}$ are the LCD modifications of (3.1):

$$\mathcal{F}_{j+\frac{1}{2}}^{\text{LCD}} = \frac{\mathbf{F}_j + \mathbf{F}_{j+1}}{2} + \mathbf{D}_{j+\frac{1}{2}}^{\text{LCD}}, \tag{3.6}$$

with the following LCD modification of the numerical diffusion term (3.2)–(3.4):

$$\begin{aligned} \mathbf{D}_{j+\frac{1}{2}}^{\text{LCD}} &= R_{j+\frac{1}{2}} P_{j+\frac{1}{2}}^{\text{LCD}} R_{j+\frac{1}{2}}^{-1} \left[\mathbf{F}_{j+\frac{1}{2}}^- - \frac{\mathbf{F}_j + \mathbf{F}_{j+1}}{2} \right] + R_{j+\frac{1}{2}} M_{j+\frac{1}{2}}^{\text{LCD}} R_{j+\frac{1}{2}}^{-1} \left[\mathbf{F}_{j+\frac{1}{2}}^+ - \frac{\mathbf{F}_j + \mathbf{F}_{j+1}}{2} \right] \\ &\quad + R_{j+\frac{1}{2}} Q_{j+\frac{1}{2}}^{\text{LCD}} \left(\mathbf{\Gamma}_{j+\frac{1}{2}}^+ - \mathbf{\Gamma}_{j+\frac{1}{2}}^- \right). \end{aligned} \tag{3.7}$$

Here,

$$\begin{aligned} P_{j+\frac{1}{2}}^{\text{LCD}} &= \text{diag}((P_1^{\text{LCD}})_{j+\frac{1}{2}}, \dots, (P_d^{\text{LCD}})_{j+\frac{1}{2}}), \quad M_{j+\frac{1}{2}}^{\text{LCD}} = \text{diag}((M_1^{\text{LCD}})_{j+\frac{1}{2}}, \dots, (M_d^{\text{LCD}})_{j+\frac{1}{2}}), \\ Q_{j+\frac{1}{2}}^{\text{LCD}} &= \text{diag}((Q_1^{\text{LCD}})_{j+\frac{1}{2}}, \dots, (Q_d^{\text{LCD}})_{j+\frac{1}{2}}) \end{aligned}$$

with

$$\begin{aligned} &((P_i^{\text{LCD}})_{j+\frac{1}{2}}, (M_i^{\text{LCD}})_{j+\frac{1}{2}}, (Q_i^{\text{LCD}})_{j+\frac{1}{2}}) \\ &= \begin{cases} \frac{1}{(\lambda_i^+)_{j+\frac{1}{2}} - (\lambda_i^-)_{j+\frac{1}{2}}} ((\lambda_i^+)_{j+\frac{1}{2}}, -(\lambda_i^-)_{j+\frac{1}{2}}, (\lambda_i^+)_{j+\frac{1}{2}} (\lambda_i^-)_{j+\frac{1}{2}}) & \text{if } (\lambda_i^+)_{j+\frac{1}{2}} - (\lambda_i^-)_{j+\frac{1}{2}} > \varepsilon, \\ 0 & \text{otherwise,} \end{cases} \end{aligned} \tag{3.8}$$

and

$$\begin{aligned} (\lambda_i^+)_{j+\frac{1}{2}} &= \max \left\{ \lambda_i(A(\mathbf{U}_{j+\frac{1}{2}}^-)), \lambda_i(A(\mathbf{U}_{j+\frac{1}{2}}^+)), 0 \right\}, \\ (\lambda_i^-)_{j+\frac{1}{2}} &= \min \left\{ \lambda_i(A(\mathbf{U}_{j+\frac{1}{2}}^-)), \lambda_i(A(\mathbf{U}_{j+\frac{1}{2}}^+)), 0 \right\}, \end{aligned}$$

for $i = 1, \dots, d$.

Finally, ε in (3.8) is a very small desingularization constant, taken $\varepsilon = 10^{-10}$ in all of the numerical examples reported in §5.

It is crucial to note that the proposed 1-D LCD-based CU scheme reduces to the second-order semi-discrete upwind scheme when applied to a linear hyperbolic system (1.2) with constant coefficients. This is proven in the following lemma.

Lemma 3.1. *If*

$$\mathbf{F}(\mathbf{U}) = \mathbf{A}\mathbf{U}, \tag{3.9}$$

where \mathbf{A} is a constant matrix, then the scheme (3.5)–(3.7) becomes the second-order semi-discrete upwind scheme.

Proof. We note that in the linear case with constant coefficients, the corresponding matrix composed of the right eigenvectors of \mathbf{A} is also a constant matrix, that is, $R_{j+\frac{1}{2}} \equiv R$, and matrices $P_{j+\frac{1}{2}}^{\text{LCD}}$ and $M_{j+\frac{1}{2}}^{\text{LCD}}$ reduce to

$$\begin{aligned} P_{j+\frac{1}{2}}^{\text{LCD}} &\equiv P = \text{diag}(\max\{\text{sign}(\lambda_1), 0\}, \dots, \max\{\text{sign}(\lambda_d), 0\}), \\ M_{j+\frac{1}{2}}^{\text{LCD}} &\equiv M = \text{diag}(\min\{\text{sign}(\lambda_1), 0\}, \dots, \min\{\text{sign}(\lambda_d), 0\}), \end{aligned} \tag{3.10}$$

while the matrix $Q_{j+\frac{1}{2}}^{\text{LCD}} \equiv 0$ as $\lambda_i^+ \lambda_i^- = \max(\lambda_i, 0) \cdot \min(\lambda_i, 0) = 0$.

Taking into account the above simplifications and substituting (3.9) and (3.10) into (3.7), yields the following expression for the numerical diffusion term:

$$\begin{aligned} \mathbf{D}_{j+\frac{1}{2}}^{\text{LCD}} &= RPR^{-1}A \left[\mathbf{U}_{j+\frac{1}{2}}^- - \frac{\bar{\mathbf{U}}_j + \bar{\mathbf{U}}_{j+1}}{2} \right] + RMR^{-1}A \left[\mathbf{U}_{j+\frac{1}{2}}^+ - \frac{\bar{\mathbf{U}}_j + \bar{\mathbf{U}}_{j+1}}{2} \right] \\ &= RPR^{-1}AR \left[R^{-1} \left(\mathbf{U}_{j+\frac{1}{2}}^- - \frac{\bar{\mathbf{U}}_j + \bar{\mathbf{U}}_{j+1}}{2} \right) \right] + RMR^{-1}AR \left[R^{-1} \left(\mathbf{U}_{j+\frac{1}{2}}^+ - \frac{\bar{\mathbf{U}}_j + \bar{\mathbf{U}}_{j+1}}{2} \right) \right] \\ &= R\Lambda^+ \left(\mathbf{\Gamma}_{j+\frac{1}{2}}^- - \frac{\mathbf{\Gamma}_j + \mathbf{\Gamma}_{j+1}}{2} \right) + R\Lambda^- \left(\mathbf{\Gamma}_{j+\frac{1}{2}}^+ - \frac{\mathbf{\Gamma}_j + \mathbf{\Gamma}_{j+1}}{2} \right), \end{aligned} \tag{3.11}$$

where

$$\begin{aligned} \Lambda^+ &= PR^{-1}AR = P\Lambda = \text{diag}(\max\{\lambda_1, 0\}, \dots, \max\{\lambda_d, 0\}), \\ \Lambda^- &= MR^{-1}AR = M\Lambda = \text{diag}(\min\{\lambda_1, 0\}, \dots, \min\{\lambda_d, 0\}). \end{aligned}$$

Finally, combining (3.9) and (3.11) together and including them into (3.6), we obtain

$$\begin{aligned} \mathcal{F}_{j+\frac{1}{2}}^{\text{LCD}} &= \frac{1}{2}A(\bar{\mathbf{U}}_j + \bar{\mathbf{U}}_{j+1}) + R\Lambda^+ \left(\Gamma_{j+\frac{1}{2}}^- - \frac{\Gamma_j + \Gamma_{j+1}}{2} \right) + R\Lambda^- \left(\Gamma_{j+\frac{1}{2}}^+ - \frac{\Gamma_j + \Gamma_{j+1}}{2} \right) \\ &= \frac{1}{2}(A^+ + A^-)(\bar{\mathbf{U}}_j + \bar{\mathbf{U}}_{j+1}) + A^+ \left(\mathbf{U}_{j+\frac{1}{2}}^- - \frac{\bar{\mathbf{U}}_j + \bar{\mathbf{U}}_{j+1}}{2} \right) + A^- \left(\mathbf{U}_{j+\frac{1}{2}}^+ - \frac{\bar{\mathbf{U}}_j + \bar{\mathbf{U}}_{j+1}}{2} \right) \\ &= A^+ \mathbf{U}_{j+\frac{1}{2}}^- + A^- \mathbf{U}_{j+\frac{1}{2}}^+, \end{aligned} \tag{3.12}$$

where $A^\pm := R\Lambda^\pm R^{-1}$. This confirms that the scheme (3.5), (3.12) is the second-order semi-discrete upwind scheme. \square

4. 2-D LCD-based central-upwind scheme

In this section, we generalize the 1-D LCD-based CU scheme introduced in §3 for the 2-D hyperbolic system of conservation laws (1.1). We design the 2-D LCD-based CU scheme in a “dimension-by-dimension” manner, so that it reads as

$$\frac{d\bar{\mathbf{U}}_{j,k}}{dt} = -\frac{\mathcal{F}_{j+\frac{1}{2},k}^{\text{LCD}} - \mathcal{F}_{j-\frac{1}{2},k}^{\text{LCD}}}{\Delta x} - \frac{\mathcal{G}_{j,k+\frac{1}{2}}^{\text{LCD}} - \mathcal{G}_{j,k-\frac{1}{2}}^{\text{LCD}}}{\Delta y}, \tag{4.1}$$

where

$$\mathcal{F}_{j+\frac{1}{2},k}^{\text{LCD}} = \frac{\mathbf{F}_{j,k} + \mathbf{F}_{j+1,k}}{2} + \mathbf{D}_{j+\frac{1}{2},k}^{\text{LCD}}, \quad \mathcal{G}_{j,k+\frac{1}{2}}^{\text{LCD}} = \frac{\mathbf{G}_{j,k} + \mathbf{G}_{j,k+1}}{2} + \mathbf{D}_{j,k+\frac{1}{2}}^{\text{LCD}}. \tag{4.2}$$

Here, $\mathbf{F}_{j,k} := \mathbf{F}(\bar{\mathbf{U}}_{j,k})$, $\mathbf{G}_{j,k} := \mathbf{G}(\bar{\mathbf{U}}_{j,k})$, and $\mathbf{D}_{j+\frac{1}{2},k}^{\text{LCD}}$ and $\mathbf{D}_{j,k+\frac{1}{2}}^{\text{LCD}}$ are the numerical diffusion terms defined by

$$\begin{aligned} \mathbf{D}_{j+\frac{1}{2},k}^{\text{LCD}} &= R_{j+\frac{1}{2},k} P_{j+\frac{1}{2},k}^{\text{LCD}} R_{j+\frac{1}{2},k}^{-1} \left[\mathbf{F}_{j,k}^E - \frac{\mathbf{F}_{j,k} + \mathbf{F}_{j+1,k}}{2} \right] \\ &\quad + R_{j+\frac{1}{2},k} M_{j+\frac{1}{2},k}^{\text{LCD}} R_{j+\frac{1}{2},k}^{-1} \left[\mathbf{F}_{j+1,k}^W - \frac{\mathbf{F}_{j,k} + \mathbf{F}_{j+1,k}}{2} \right] + R_{j+\frac{1}{2},k} Q_{j+\frac{1}{2},k}^{\text{LCD}} \left(\Gamma_{j+1,k}^W - \Gamma_{j,k}^E \right), \\ \mathbf{D}_{j,k+\frac{1}{2}}^{\text{LCD}} &= R_{j,k+\frac{1}{2}} P_{j,k+\frac{1}{2}}^{\text{LCD}} R_{j,k+\frac{1}{2}}^{-1} \left[\mathbf{G}_{j,k}^N - \frac{\mathbf{G}_{j,k} + \mathbf{G}_{j,k+1}}{2} \right] \\ &\quad + R_{j,k+\frac{1}{2}} M_{j,k+\frac{1}{2}}^{\text{LCD}} R_{j,k+\frac{1}{2}}^{-1} \left[\mathbf{G}_{j,k+1}^S - \frac{\mathbf{G}_{j,k} + \mathbf{G}_{j,k+1}}{2} \right] + R_{j,k+\frac{1}{2}} Q_{j,k+\frac{1}{2}}^{\text{LCD}} \left[\Gamma_{j,k+1}^S - \Gamma_{j,k}^N \right]. \end{aligned} \tag{4.3}$$

The matrices $R_{j+\frac{1}{2},k}$, $R_{j+\frac{1}{2},k}^{-1}$ and $R_{j,k+\frac{1}{2}}$, $R_{j,k+\frac{1}{2}}^{-1}$ are the matrices such that $R_{j+\frac{1}{2},k}^{-1} \hat{A}_{j+\frac{1}{2},k} R_{j+\frac{1}{2},k}$ and $R_{j,k+\frac{1}{2}}^{-1} \hat{B}_{j,k+\frac{1}{2}} R_{j,k+\frac{1}{2}}$ are diagonal. Here, $\hat{A}_{j+\frac{1}{2},k} = A(\hat{\mathbf{U}}_{j+\frac{1}{2},k})$, $\hat{B}_{j,k+\frac{1}{2}} = B(\hat{\mathbf{U}}_{j,k+\frac{1}{2}})$ with $A(\mathbf{U}) = \frac{\partial \mathbf{F}(\mathbf{U})}{\partial \mathbf{U}}$, $B(\mathbf{U}) = \frac{\partial \mathbf{G}(\mathbf{U})}{\partial \mathbf{U}}$, and $\hat{\mathbf{U}}_{j+\frac{1}{2},k}$, $\hat{\mathbf{U}}_{j,k+\frac{1}{2}}$ are either simple averages $(\bar{\mathbf{U}}_{j,k} + \bar{\mathbf{U}}_{j+1,k})/2$, $(\bar{\mathbf{U}}_{j,k} + \bar{\mathbf{U}}_{j,k+1})/2$ or another type of averages of $\bar{\mathbf{U}}_{j,k}$, $\bar{\mathbf{U}}_{j+1,k}$ and $\bar{\mathbf{U}}_{j,k}$, $\bar{\mathbf{U}}_{j,k+1}$ states, respectively. The numerical fluxes $\mathbf{F}_{j,k}^{\text{E,W}}$ and $\mathbf{G}_{j,k}^{\text{N,S}}$ are defined by $\mathbf{F}_{j,k}^{\text{E,W}} := \mathbf{F}(\mathbf{U}_{j,k}^{\text{E,W}})$, $\mathbf{G}_{j,k}^{\text{N,S}} := \mathbf{G}(\mathbf{U}_{j,k}^{\text{N,S}})$, and the details of reconstructing the point values $\mathbf{U}_{j,k}^{\text{E,W}}$ and $\mathbf{U}_{j,k}^{\text{N,S}}$, $\Gamma_{j,k}^{\text{E,W}}$ and $\Gamma_{j,k}^{\text{N,S}}$ for the 2-D Euler equations of gas dynamics are provided in Appendix C. Finally, the diagonal matrices $P_{j+\frac{1}{2},k}^{\text{LCD}}$, $M_{j+\frac{1}{2},k}^{\text{LCD}}$, $Q_{j+\frac{1}{2},k}^{\text{LCD}}$, $P_{j,k+\frac{1}{2}}^{\text{LCD}}$, $M_{j,k+\frac{1}{2}}^{\text{LCD}}$, and $Q_{j,k+\frac{1}{2}}^{\text{LCD}}$ are defined by

$$\begin{aligned} P_{j+\frac{1}{2},k}^{\text{LCD}} &= \text{diag} \left((P_1^{\text{LCD}})_{j+\frac{1}{2},k}, \dots, (P_d^{\text{LCD}})_{j+\frac{1}{2},k} \right), & P_{j,k+\frac{1}{2}}^{\text{LCD}} &= \text{diag} \left((P_1^{\text{LCD}})_{j,k+\frac{1}{2}}, \dots, (P_d^{\text{LCD}})_{j,k+\frac{1}{2}} \right), \\ M_{j+\frac{1}{2},k}^{\text{LCD}} &= \text{diag} \left((M_1^{\text{LCD}})_{j+\frac{1}{2},k}, \dots, (M_d^{\text{LCD}})_{j+\frac{1}{2},k} \right), & M_{j,k+\frac{1}{2}}^{\text{LCD}} &= \text{diag} \left((M_1^{\text{LCD}})_{j,k+\frac{1}{2}}, \dots, (M_d^{\text{LCD}})_{j,k+\frac{1}{2}} \right), \\ Q_{j+\frac{1}{2},k}^{\text{LCD}} &= \text{diag} \left((Q_1^{\text{LCD}})_{j+\frac{1}{2},k}, \dots, (Q_d^{\text{LCD}})_{j+\frac{1}{2},k} \right), & Q_{j,k+\frac{1}{2}}^{\text{LCD}} &= \text{diag} \left((Q_1^{\text{LCD}})_{j,k+\frac{1}{2}}, \dots, (Q_d^{\text{LCD}})_{j,k+\frac{1}{2}} \right), \end{aligned}$$

where for all $i = 1, \dots, d$

$$\begin{aligned} & \left((P_i^{\text{LCD}})_{j+\frac{1}{2},k}, (M_i^{\text{LCD}})_{j+\frac{1}{2},k}, (Q_i^{\text{LCD}})_{j+\frac{1}{2},k} \right) \\ &= \begin{cases} \frac{1}{\Delta(\lambda_i)_{j+\frac{1}{2},k}} \left((\lambda_i^+)_{j+\frac{1}{2},k}, -(\lambda_i^-)_{j+\frac{1}{2},k}, (\lambda_i^+)_{j+\frac{1}{2},k}(\lambda_i^-)_{j+\frac{1}{2},k} \right) & \text{if } \Delta(\lambda_i)_{j+\frac{1}{2},k} > \varepsilon, \\ 0 & \text{otherwise,} \end{cases} \\ & \left((P_i^{\text{LCD}})_{j,k+\frac{1}{2}}, (M_i^{\text{LCD}})_{j,k+\frac{1}{2}}, (Q_i^{\text{LCD}})_{j,k+\frac{1}{2}} \right) \\ &= \begin{cases} \frac{1}{\Delta(\mu_i)_{j,k+\frac{1}{2}}} \left((\mu_i^+)_{j,k+\frac{1}{2}}, -(\mu_i^-)_{j,k+\frac{1}{2}}, (\mu_i^+)_{j,k+\frac{1}{2}}(\mu_i^-)_{j,k+\frac{1}{2}} \right) & \text{if } \Delta(\mu_i)_{j,k+\frac{1}{2}} > \varepsilon, \\ 0 & \text{otherwise.} \end{cases} \end{aligned}$$

Here, $\Delta(\lambda_i)_{j+\frac{1}{2},k} := (\lambda_i^+)_{j+\frac{1}{2},k} - (\lambda_i^-)_{j+\frac{1}{2},k}$, $\Delta(\mu_i)_{j,k+\frac{1}{2}} := (\mu_i^+)_{j,k+\frac{1}{2}} - (\mu_i^-)_{j,k+\frac{1}{2}}$, and

$$\begin{aligned} (\lambda_i^+)_{j+\frac{1}{2},k} &= \max \left\{ \lambda_i(A(\mathbf{U}_{j,k}^E)), \lambda_i(A(\mathbf{U}_{j+1,k}^W)), 0 \right\}, \\ (\lambda_i^-)_{j+\frac{1}{2},k} &= \min \left\{ \lambda_i(A(\mathbf{U}_{j,k}^E)), \lambda_i(A(\mathbf{U}_{j+1,k}^W)), 0 \right\}, \\ (\mu_i^+)_{j,k+\frac{1}{2}} &= \max \left\{ \mu_i(B(\mathbf{U}_{j,k}^N)), \mu_i(B(\mathbf{U}_{j,k+1}^S)), 0 \right\}, \\ (\mu_i^-)_{j,k+\frac{1}{2}} &= \min \left\{ \mu_i(B(\mathbf{U}_{j,k}^N)), \mu_i(B(\mathbf{U}_{j,k+1}^S)), 0 \right\}, \end{aligned}$$

where λ_i and μ_i are the eigenvalues of the Jacobians $A(\mathbf{U})$ and $B(\mathbf{U})$: $\lambda_1(A) \leq \dots \leq \lambda_d(A)$ and $\mu_1(B) \leq \dots \leq \mu_d(B)$, respectively.

We note that as in the 1-D case, the proposed 2-D LCD-based CU scheme reduces to the second-order semi-discrete upwind scheme when applied to a linear hyperbolic system

$$\mathbf{U}_t + A\mathbf{U}_x + B\mathbf{U}_y = \mathbf{0}$$

with constant matrices A and B . This is proven in the following lemma.

Lemma 4.1. *If*

$$\mathbf{F}(\mathbf{U}) = A\mathbf{U} \quad \text{and} \quad \mathbf{G}(\mathbf{U}) = B\mathbf{U}, \tag{4.4}$$

where A and B are constant matrices, then the scheme (4.1)–(4.3) becomes the second-order semi-discrete upwind scheme.

Proof. As in Lemma 3.1, we note that the corresponding matrices composed of the right eigenvectors of A and B are also constant matrices, that is, $R_{j+\frac{1}{2},k} \equiv R_1$, $R_{j,k+\frac{1}{2}} \equiv R_2$ and matrices $P_{j+\frac{1}{2},k}^{\text{LCD}}$, $P_{j,k+\frac{1}{2}}^{\text{LCD}}$, $M_{j+\frac{1}{2},k}^{\text{LCD}}$ and $M_{j,k+\frac{1}{2}}^{\text{LCD}}$ reduce to

$$\begin{aligned} P_{j+\frac{1}{2},k}^{\text{LCD}} &\equiv P_1 = \text{diag}(\max\{\text{sign}(\lambda_1), 0\}, \dots, \max\{\text{sign}(\lambda_d), 0\}), \\ P_{j,k+\frac{1}{2}}^{\text{LCD}} &\equiv P_2 = \text{diag}(\max\{\text{sign}(\mu_1), 0\}, \dots, \max\{\text{sign}(\mu_d), 0\}), \\ M_{j+\frac{1}{2},k}^{\text{LCD}} &\equiv M_1 = \text{diag}(\min\{\text{sign}(\lambda_1), 0\}, \dots, \min\{\text{sign}(\lambda_d), 0\}), \\ M_{j,k+\frac{1}{2}}^{\text{LCD}} &\equiv M_2 = \text{diag}(\min\{\text{sign}(\mu_1), 0\}, \dots, \min\{\text{sign}(\mu_d), 0\}), \end{aligned} \tag{4.5}$$

while the matrices $Q_{j+\frac{1}{2},k}^{\text{LCD}} = Q_{j,k+\frac{1}{2}}^{\text{LCD}} \equiv 0$ as $\lambda_i^+ \lambda_i^- = \max(\lambda_i, 0) \cdot \min(\lambda_i, 0) = 0$ and $\mu_i^+ \mu_i^- = \max(\mu_i, 0) \cdot \min(\mu_i, 0) = 0$.

Taking into account the above simplifications and substituting (4.4) and (4.5) into (4.3), yields the following expressions for the numerical diffusion terms in the x - and y -directions, respectively:

$$\begin{aligned}
 \mathbf{D}_{j+\frac{1}{2},k}^{\text{LCD}} &= R_1 P_1 R_1^{-1} A \left[\mathbf{U}_{j,k}^E - \frac{\bar{\mathbf{U}}_{j,k} + \bar{\mathbf{U}}_{j+1,k}}{2} \right] + R_1 M_1 R_1^{-1} A \left[\mathbf{U}_{j+1,k}^W - \frac{\bar{\mathbf{U}}_{j,k} + \bar{\mathbf{U}}_{j+1,k}}{2} \right] \\
 &= R_1 P_1 R_1^{-1} A R_1 \left[R_1^{-1} \left(\mathbf{U}_{j,k}^E - \frac{\bar{\mathbf{U}}_{j,k} + \bar{\mathbf{U}}_{j+1,k}}{2} \right) \right] \\
 &\quad + R_1 M_1 R_1^{-1} A R_1 \left[R_1^{-1} \left(\mathbf{U}_{j+1,k}^W - \frac{\bar{\mathbf{U}}_{j,k} + \bar{\mathbf{U}}_{j+1,k}}{2} \right) \right] \\
 &= R_1 \Lambda_1^+ \left(\mathbf{\Gamma}_{j,k}^E - \frac{\mathbf{\Gamma}_{j,k} + \mathbf{\Gamma}_{j+1,k}}{2} \right) + R_1 \Lambda_1^- \left(\mathbf{\Gamma}_{j+1,k}^W - \frac{\mathbf{\Gamma}_{j,k} + \mathbf{\Gamma}_{j+1,k}}{2} \right), \\
 \mathbf{D}_{j,k+\frac{1}{2}}^{\text{LCD}} &= R_2 P_2 R_2^{-1} B \left[\mathbf{U}_{j,k}^N - \frac{\bar{\mathbf{U}}_{j,k} + \bar{\mathbf{U}}_{j,k+1}}{2} \right] + R_2 M_2 R_2^{-1} B \left[\mathbf{U}_{j,k+1}^S - \frac{\bar{\mathbf{U}}_{j,k} + \bar{\mathbf{U}}_{j,k+1}}{2} \right] \\
 &= R_2 P_2 R_2^{-1} B R_2 \left[R_2^{-1} \left(\mathbf{U}_{j,k}^N - \frac{\bar{\mathbf{U}}_{j,k} + \bar{\mathbf{U}}_{j,k+1}}{2} \right) \right] \\
 &\quad + R_2 M_2 R_2^{-1} B R_2 \left[R_2^{-1} \left(\mathbf{U}_{j,k+1}^S - \frac{\bar{\mathbf{U}}_{j,k} + \bar{\mathbf{U}}_{j,k+1}}{2} \right) \right] \\
 &= R_2 \Lambda_2^+ \left(\mathbf{\Gamma}_{j,k}^N - \frac{\mathbf{\Gamma}_{j,k} + \mathbf{\Gamma}_{j,k+1}}{2} \right) + R_2 \Lambda_2^- \left(\mathbf{\Gamma}_{j,k+1}^S - \frac{\mathbf{\Gamma}_{j,k} + \mathbf{\Gamma}_{j,k+1}}{2} \right),
 \end{aligned} \tag{4.6}$$

where

$$\begin{aligned}
 \Lambda_1^+ &= P_1 R_1^{-1} A R_1 = P_1 \Lambda_1 = \text{diag}(\max\{\lambda_1, 0\}, \dots, \max\{\lambda_d, 0\}), \\
 \Lambda_1^- &= M_1 R_1^{-1} A R_1 = M_1 \Lambda_1 = \text{diag}(\min\{\lambda_1, 0\}, \dots, \min\{\lambda_d, 0\}), \\
 \Lambda_2^+ &= P_2 R_2^{-1} B R_2 = P_2 \Lambda_2 = \text{diag}(\max\{\mu_1, 0\}, \dots, \max\{\mu_d, 0\}), \\
 \Lambda_2^- &= M_2 R_2^{-1} B R_2 = M_2 \Lambda_2 = \text{diag}(\min\{\mu_1, 0\}, \dots, \min\{\mu_d, 0\}).
 \end{aligned}$$

Finally, combining (4.4) and (4.6) together and including them into (4.2), we obtain

$$\begin{aligned}
 \mathcal{F}_{j+\frac{1}{2},k}^{\text{LCD}} &= \frac{1}{2} A (\bar{\mathbf{U}}_{j,k} + \bar{\mathbf{U}}_{j+1,k}) \\
 &\quad + R_1 \Lambda_1^+ \left(\mathbf{\Gamma}_{j,k}^E - \frac{\mathbf{\Gamma}_{j,k} + \mathbf{\Gamma}_{j+1,k}}{2} \right) + R_1 \Lambda_1^- \left(\mathbf{\Gamma}_{j+1,k}^W - \frac{\mathbf{\Gamma}_{j,k} + \mathbf{\Gamma}_{j+1,k}}{2} \right) \\
 &= \frac{1}{2} (A^+ + A^-) (\bar{\mathbf{U}}_{j,k} + \bar{\mathbf{U}}_{j+1,k}) \\
 &\quad + A^+ \left(\mathbf{U}_{j,k}^E - \frac{\bar{\mathbf{U}}_{j,k} + \bar{\mathbf{U}}_{j+1,k}}{2} \right) + A^- \left(\mathbf{U}_{j+1,k}^W - \frac{\bar{\mathbf{U}}_{j,k} + \bar{\mathbf{U}}_{j+1,k}}{2} \right) = A^+ \mathbf{U}_{j,k}^E + A^- \mathbf{U}_{j+1,k}^W,
 \end{aligned} \tag{4.7}$$

$$\begin{aligned}
 \mathcal{G}_{j,k+\frac{1}{2}}^{\text{LCD}} &= \frac{1}{2} B (\bar{\mathbf{U}}_{j,k} + \bar{\mathbf{U}}_{j,k+1}) \\
 &\quad + R_2 \Lambda_2^+ \left(\mathbf{\Gamma}_{j,k}^N - \frac{\mathbf{\Gamma}_{j,k} + \mathbf{\Gamma}_{j,k+1}}{2} \right) + R_2 \Lambda_2^- \left(\mathbf{\Gamma}_{j,k+1}^S - \frac{\mathbf{\Gamma}_{j,k} + \mathbf{\Gamma}_{j,k+1}}{2} \right) \\
 &= \frac{1}{2} (B^+ + B^-) (\bar{\mathbf{U}}_{j,k} + \bar{\mathbf{U}}_{j,k+1}) \\
 &\quad + B^+ \left(\mathbf{U}_{j,k}^N - \frac{\bar{\mathbf{U}}_{j,k} + \bar{\mathbf{U}}_{j,k+1}}{2} \right) + B^- \left(\mathbf{U}_{j,k+1}^S - \frac{\bar{\mathbf{U}}_{j,k} + \bar{\mathbf{U}}_{j,k+1}}{2} \right) = B^+ \mathbf{U}_{j,k}^N + B^- \mathbf{U}_{j,k+1}^S,
 \end{aligned} \tag{4.8}$$

where $A^\pm := R_1 \Lambda_1^\pm R_1^{-1}$ and $B^\pm := R_2 \Lambda_2^\pm R_2^{-1}$. This confirms that the scheme (4.1), (4.7)–(4.8) is the second-order semi-discrete upwind scheme. \square

5. Numerical examples

In this section, we apply the proposed LCD-based CU schemes, which will be referred to as the New CU schemes, to the 1-D and 2-D Euler equations of gas dynamics described in Appendices A and C, respectively. We conduct several numerical

Table 5.1

Example 1: The L^1 -errors and experimental convergence rates for the density (ρ), momentum (ρu), and total energy (E).

Δx	ρ		ρu		E	
	Error	Rate	Error	Rate	Error	Rate
1/200	2.72e-04	2.02	7.88e-04	2.02	3.55e-03	2.02
1/400	6.60e-05	2.08	1.92e-04	2.07	8.64e-04	2.07
1/800	1.59e-05	2.01	4.64e-05	2.01	2.08e-04	2.01
1/1600	3.93e-06	2.04	1.15e-05	2.03	5.15e-05	2.04
1/3200	9.62e-07	2.01	2.82e-06	2.01	1.26e-05	2.01

Table 5.2

Example 2: The L^∞ -errors for the velocity (u) and pressure (p) between the exact solutions.

Δx	$\ u - u_{\text{Exact}}\ _\infty$	$\ p - p_{\text{Exact}}\ _\infty$
1/200	1.25e-16	2.22e-16

experiments and compare the performance of the *New CU* schemes with that of the corresponding 1-D and 2-D second-order CU schemes from [18] and [22], respectively, which will be referred to as the *Old CU* schemes.

In Examples 1–11, we take the specific heat ratio $\gamma = 1.4$, while in Example 12, we set $\gamma = 5/3$. In all of the examples, we use the CFL number 0.4.

5.1. One-dimensional examples

Example 1—1-D accuracy test

In the first example, we consider the problem with the following smooth initial data:

$$u(x, 0) = \sin\left(\frac{\pi x}{5} + \frac{\pi}{4}\right), \quad \rho(x, 0) = \left[\frac{\gamma - 1}{2\sqrt{\gamma}}(u(x, 0) + 10)\right]^{\frac{2}{\gamma-1}}, \quad p(x, 0) = \rho^\gamma(x, 0).$$

We implement the periodic boundary conditions on the computational domain $[0, 10]$ and compute the numerical solution until the final time $t = 0.1$ (at which the solution is still smooth) using the *New CU* scheme on a sequence of uniform meshes with $\Delta x = 1/50, 1/100, 1/200, 1/400, 1/800, 1/1600,$ and $1/3200$.

We compute L^1 -errors and estimate the experimental convergence rates using the following Runge formulae, which are based on the solutions computed on the three consecutive uniform grids with the mesh sizes $\Delta x, 2\Delta x,$ and $4\Delta x$ and denoted by $(\cdot)^{\Delta x}, (\cdot)^{2\Delta x},$ and $(\cdot)^{4\Delta x},$ respectively:

$$\text{Error}(\Delta x) \approx \frac{\delta_{24}^2}{|\delta_{12} - \delta_{24}|}, \quad \text{Rate}(\Delta x) \approx \log_2\left(\frac{\delta_{24}}{\delta_{12}}\right).$$

Here, $\delta_{12} := \|(\cdot)^{\Delta x} - (\cdot)^{2\Delta x}\|_{L^1}$ and $\delta_{24} := \|(\cdot)^{2\Delta x} - (\cdot)^{4\Delta x}\|_{L^1}$. The obtained results for the density, momentum, and total energy are reported in Table 5.1, where one can clearly see that the second order of accuracy is achieved.

Example 2—moving contact wave

In the second, we consider the moving contact discontinuity problem from [20], which is considered on the interval $[0, 1]$ with the free boundary conditions at both ends and subject to the following initial conditions:

$$(\rho, u, p)(x, 0) = \begin{cases} (1.4, 0.1, 1), & x < 0.5, \\ (1, 0.1, 1), & x > 0.5. \end{cases}$$

We compute the numerical solutions until the final time $t = 0.2$ by both the *New* and *Old CU* schemes on a uniform mesh with $\Delta x = 1/200$ and then plot them in Fig. 5.1 together with the exact solution. As one can see, the *New CU* scheme achieves slightly higher resolution than the *Old* one. It is also instructive to note that both the velocity u and pressure p computed by the *New CU* scheme, remain constant in this example. We illustrate it in Table 5.2, where we show that both u and p are computed within the machine error. Moreover, this property is true for any problem with initially constant u and p as stated in the following lemma.

Lemma 5.1. *If $u(x, 0) \equiv \check{u}, p(x, 0) \equiv \check{p}$, where \check{u} and $\check{p} > 0$ are given constants, then $u(x, t) \equiv \check{u}$ and $p(x, t) \equiv \check{p}$ for all t .*

The proof of this lemma is given in Appendix B.

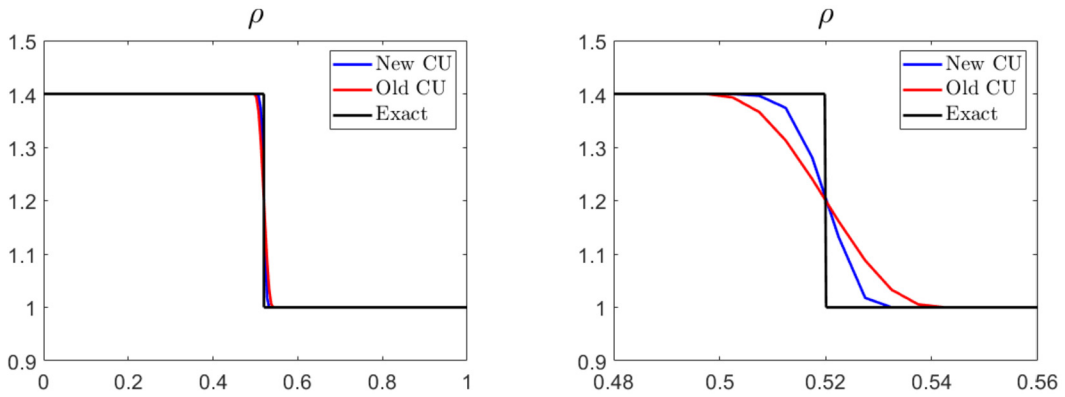


Fig. 5.1. Example 2: Density (ρ) computed by the New and Old CU schemes (left) and zoom at $x \in [0.48, 0.56]$ (right).

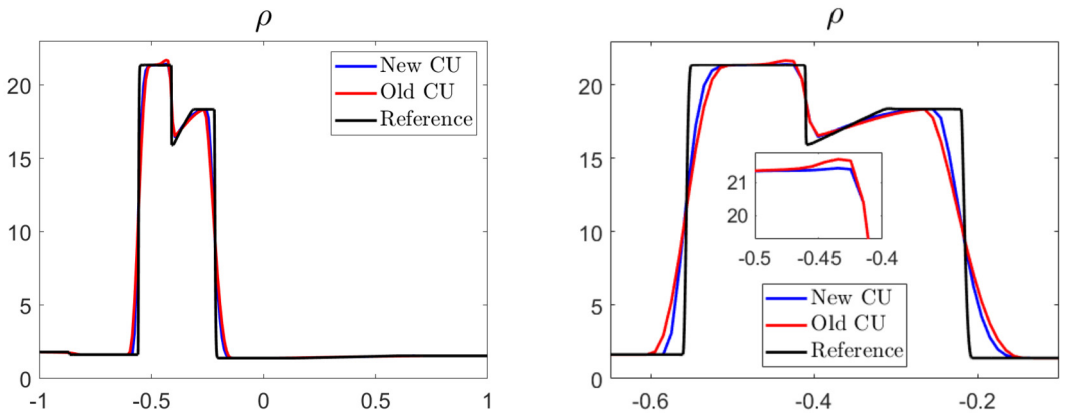


Fig. 5.2. Example 3: Density (ρ) computed by the New and Old CU schemes and zoom at $x \in [-0.65, -0.1]$.

Example 3—“shock-bubble” interaction problem

In the third example, we consider the “shock-bubble” interaction problem taken from [23]. The initial data, given by

$$(\rho, u, p)(x, 0) = \begin{cases} (13.1538, 0, 1) & \text{if } |x| < 0.25, \\ (1.3333, -0.3535, 1.5) & \text{if } x > 0.75, \\ (1, 0, 1) & \text{otherwise,} \end{cases}$$

correspond to a left-moving shock, initially located at $x = 0.75$, and a bubble of radius 0.25, initially located at the origin. We implement solid wall boundary conditions on the left and free boundary conditions on the right of the computational domain $[-1, 1]$. We compute the numerical solution until the final time $t = 3$ using both the New and Old CU schemes on the uniform mesh with $\Delta x = 1/100$. The obtained numerical results are presented in Fig. 5.2 along with the reference solution computed by the Old CU scheme on a much finer mesh with $\Delta x = 1/2000$. As one can see, the results obtained by the New CU scheme are sharper and less oscillatory compared to the Old CU scheme results, which have lower resolution of the shock waves and contain an oscillation at the contact discontinuity.

Example 4—shock-entropy wave interaction problem

In this example, we consider the shock-entropy problem from [40]. The initial conditions,

$$(\rho, u, p)(x, 0) = \begin{cases} (1.51695, 0.523346, 1.805), & x < -4.5, \\ (1 + 0.1 \sin(20x), 0, 1), & x > -4.5, \end{cases}$$

correspond to a forward-facing shock wave of Mach 1.1 interacting with high-frequency density perturbations, that is, as the shock wave moves, the perturbations spread ahead. We set free boundary condition at the both ends of the computational domain $[-5, 5]$. We apply both New and Old CU schemes and compute the solutions until the final time $t = 5$ on a uniform mesh with $\Delta x = 1/80$. The numerical results are shown in Fig. 5.3 along with the reference solution computed by the Old CU scheme on a much finer mesh with $\Delta x = 1/400$. One can observe that the New CU scheme produces substantially more accurate results compared to those obtained by the Old CU scheme. This can also be clearly seen on Fig. 5.3 (right), where we zoom at the area where the solution has smooth oscillatory structures.

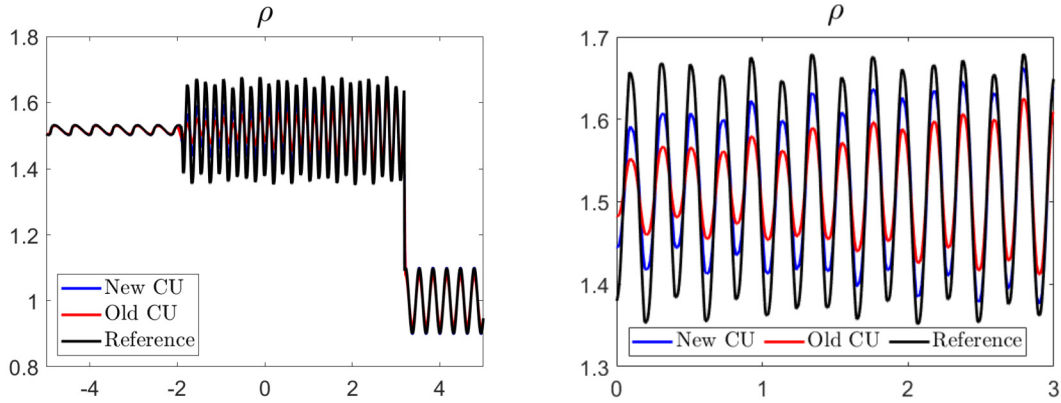


Fig. 5.3. Example 4: Density (ρ) computed by the New and Old CU schemes and zoom at $x \in [0, 3]$.

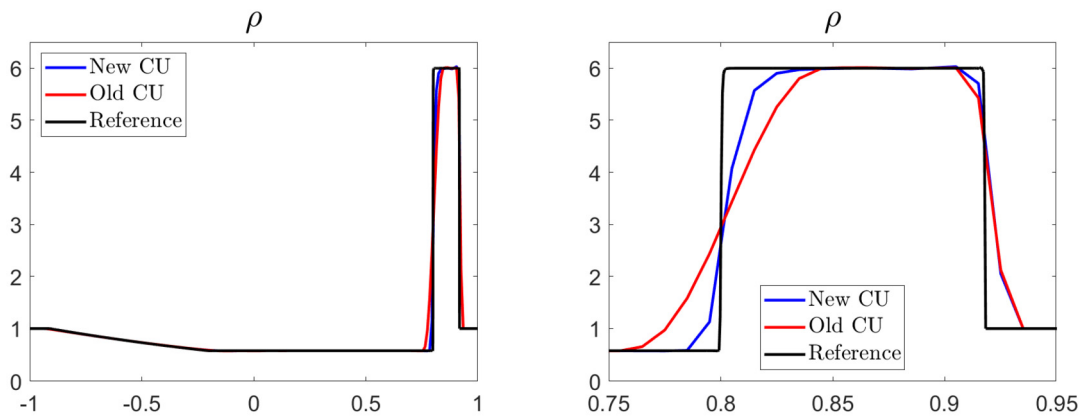


Fig. 5.4. Example 5: Density (ρ) computed by the New and Old CU schemes and zoom at $x \in [0.75, 0.95]$.

Example 5—stationary contact wave, traveling shock and rarefaction wave

In the fifth example, we consider the strong shocks interaction problem proposed in [45]. The initial conditions,

$$(\rho, u, p)(x, 0) = \begin{cases} (1, -19.59745, 1000) & \text{if } x < 0.8, \\ (1, -19.59745, 0.01) & \text{otherwise,} \end{cases}$$

are prescribed in the computational domain $[-1, 1]$, in which free boundary conditions are implemented. We compute the numerical solutions until the final time $t = 0.03$ by both the New and Old CU schemes on a uniform mesh with $\Delta x = 1/100$, as well as the reference solution, which is obtained by the Old CU scheme on a much finer mesh with $\Delta x = 1/2000$. The numerical results, plotted in Fig. 5.4, show that both schemes produce non-oscillatory numerical solutions, but the resolution of the contact wave achieved by the New CU scheme is higher; see also Fig. 5.4 (right), where we zoom at the neighborhood of the contact wave.

Example 6—blast wave problem

In the last 1-D example, we solve the strong shocks interaction problem from [45], which is considered on the interval $[0, 1]$ with the solid wall boundary conditions at both ends and subject to the following initial conditions:

$$(\rho, u, p)(x, 0) = \begin{cases} (1, 0, 1000), & x < 0.1, \\ (1, 0, 0.01), & 0.1 \leq x \leq 0.9, \\ (1, 0, 100), & x > 0.9. \end{cases}$$

We compute the numerical solutions until the final time $t = 0.038$ by both the New and Old CU schemes on a uniform mesh with $\Delta x = 1/400$ and implement the Old CU scheme on a fine grid with $\Delta x = 1/4000$ to obtain the corresponding reference solution. The obtained results, presented in Fig. 5.5, demonstrate that the New CU scheme achieves slightly higher resolution of the second density spike.

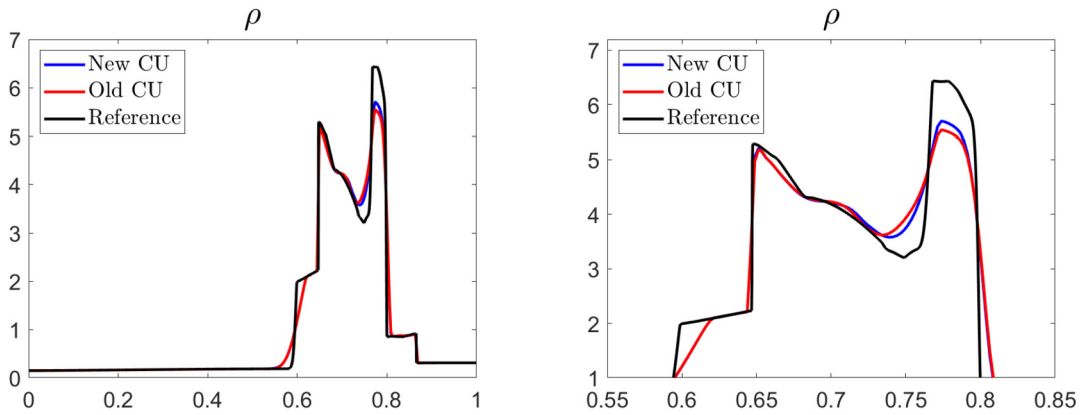


Fig. 5.5. Example 6: Density (ρ) computed by the New and Old CU schemes and zoom at $x \in [0.55, 0.85]$.

Table 5.3

Example 7: The L^1 -errors and experimental convergence rates for the density (ρ).

$\Delta x = \Delta y$	Error	Rate
1/50	1.76e-04	—
1/100	4.05e-05	2.12
1/200	8.86e-06	2.19
1/400	1.92e-06	2.20

5.2. Two-dimensional examples

Example 7—2-D accuracy test

In the first 2-D example taken from [19], we consider the 2-D Euler equations of gas dynamics subject to the periodic initial conditions,

$$\rho(x, y, 0) = 1 + \frac{1}{2} \sin(\pi(x + y)), \quad u(x, y, 0) \equiv 1, \quad v(x, y, 0) \equiv -0.7, \quad p(x, y, 0) \equiv 1,$$

prescribed on $[-1, 1] \times [-1, 1]$. The exact solution of this initial value problem can be easily obtained and it is given by

$$\rho(x, y, t) = 1 + \frac{1}{2} \sin[\pi(x + y - 0.3t)], \quad u(x, y, t) \equiv 1, \quad v(x, y, t) \equiv -0.7, \quad p(x, y, t) \equiv 1.$$

We first compute the numerical solution until the final time $t = 0.1$ using the New CU scheme on a sequence of uniform meshes with $\Delta x = \Delta y = 1/50, 1/100, 1/200,$ and $1/400$. We then measure the L^1 -errors and the corresponding experimental convergence rates for the density. The obtained results presented in Table 5.3, confirm that the New CU scheme achieves the expected second order of accuracy.

Example 8—2-D Riemann problem

In the second 2-D example, we consider Configuration 3 of the 2-D Riemann problems taken from [22]; see also [36,37,46]. The initial conditions,

$$(\rho(x, y, 0), u(x, y, 0), v(x, y, 0), p(x, y, 0)) = \begin{cases} (1.5, 0, 0, 1.5), & x > 1, y > 1, \\ (0.5323, 1.206, 0, 0.3), & x < 1, y > 1, \\ (0.138, 1.206, 1.206, 0.029), & x < 1, y < 1, \\ (0.5323, 0, 1.206, 0.3), & x > 1, y < 1, \end{cases}$$

are prescribed in the computational domain $[0, 1.2] \times [0, 1.2]$, in which the free boundary conditions are implemented on all of the four sides of the domain. We compute the numerical solutions until the final time $t = 1$ by both the New and Old CU schemes on a uniform mesh with $\Delta x = \Delta y = 3/2500$, and plot the obtained results in Fig. 5.6. As one can clearly see, the New CU scheme outperforms the Old CU scheme in capturing a sideband instability of the jet in the zones of strong along-jet velocity shear and the instability along the jet's neck.

Example 9—explosion problem

In this example, we consider the explosion problem studied in [8,17,20,29]. This is a circularly symmetric problem with an initial circular region of higher density and pressure with the following initial conditions,

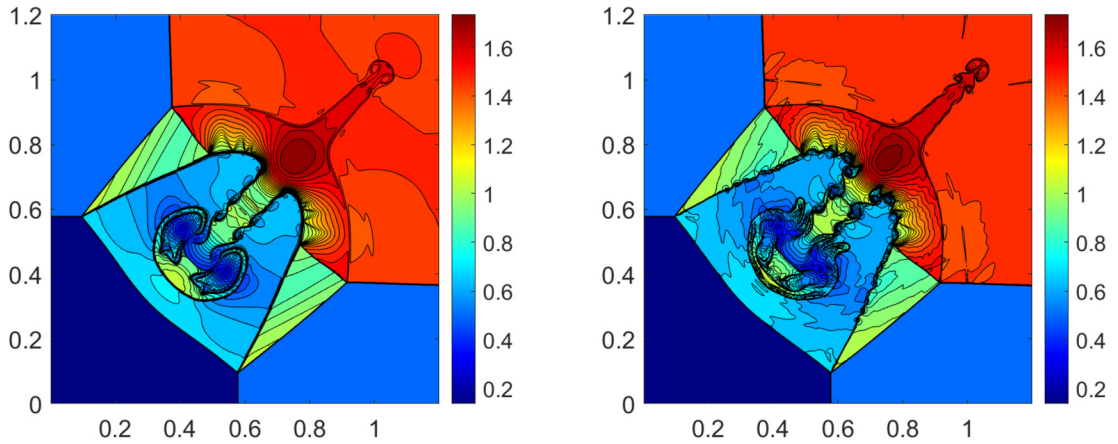


Fig. 5.6. Example 8: Density (ρ) computed by the Old (left) and New (right) CU schemes.

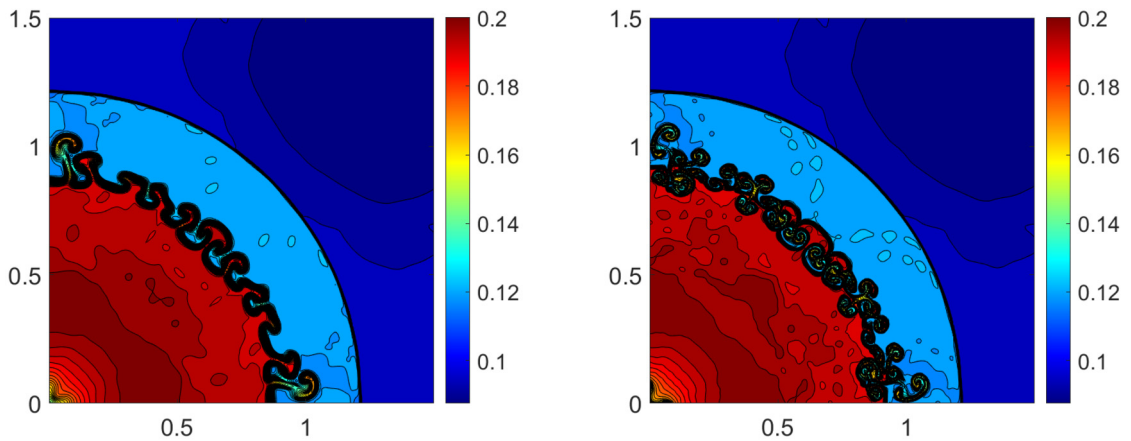


Fig. 5.7. Example 9: Density (ρ) computed by the Old (left) and New (right) CU schemes.

$$(\rho(x, y, 0), u(x, y, 0), v(x, y, 0), p(x, y, 0)) = \begin{cases} (1, 0, 0, 1), & x^2 + y^2 < 0.16, \\ (0.125, 0, 0, 0.1), & \text{otherwise,} \end{cases}$$

prescribed in the computational domain $[0, 1.5] \times [0, 1.5]$. Solid wall boundary conditions are imposed at $x = 0$ and $y = 0$, while free boundary conditions are set at $x = 1.5$ and $y = 1.5$. It is well-known that the solution of this initial-boundary value problem develops circular shock and contact waves. While the shock wave is stable and a good numerical scheme should contain a sufficient amount of numerical dissipation to capture the shock in a stable, non-oscillatory manner, the contact wave is unstable and can only be stabilized numerically by the numerical diffusion present in the scheme. Therefore, this is a good benchmark to measure the amount of numerical dissipation present in different schemes as one ideally wants to have as little numerical dissipation as possible, but sufficient to stabilize the shock wave.

We apply both New and Old CU schemes and compute the numerical solutions on a uniform mesh with $\Delta x = \Delta y = 3/800$ until the final time $t = 3.2$. The obtained results are presented in Fig. 5.7. One can observe that compared with the results obtained by the Old CU scheme, the contact curve captured by the New CU scheme is substantially “curlier” and the mixing layer is slightly wider (indicating a more severe instability), while the shock is still stable.

Example 10—implosion problem

In this example, we consider the implosion problem taken from [8,17,20,29]. The initial conditions,

$$(\rho(x, y, 0), u(x, y, 0), v(x, y, 0), p(x, y, 0)) = \begin{cases} (0.125, 0, 0, 0.14), & |x| + |y| < 0.15, \\ (1, 0, 0, 1), & \text{otherwise,} \end{cases}$$

are prescribed in the computational domain $[0, 0.3] \times [0, 0.3]$ with solid boundary conditions imposed at all of the four sides. We compute the numerical solutions until the final time $t = 2.5$ by both the New and Old CU schemes on a uniform mesh with $\Delta x = \Delta y = 1/2000$. The obtained results are depicted in Fig. 5.8 (top row). As one can clearly see, a jet generated

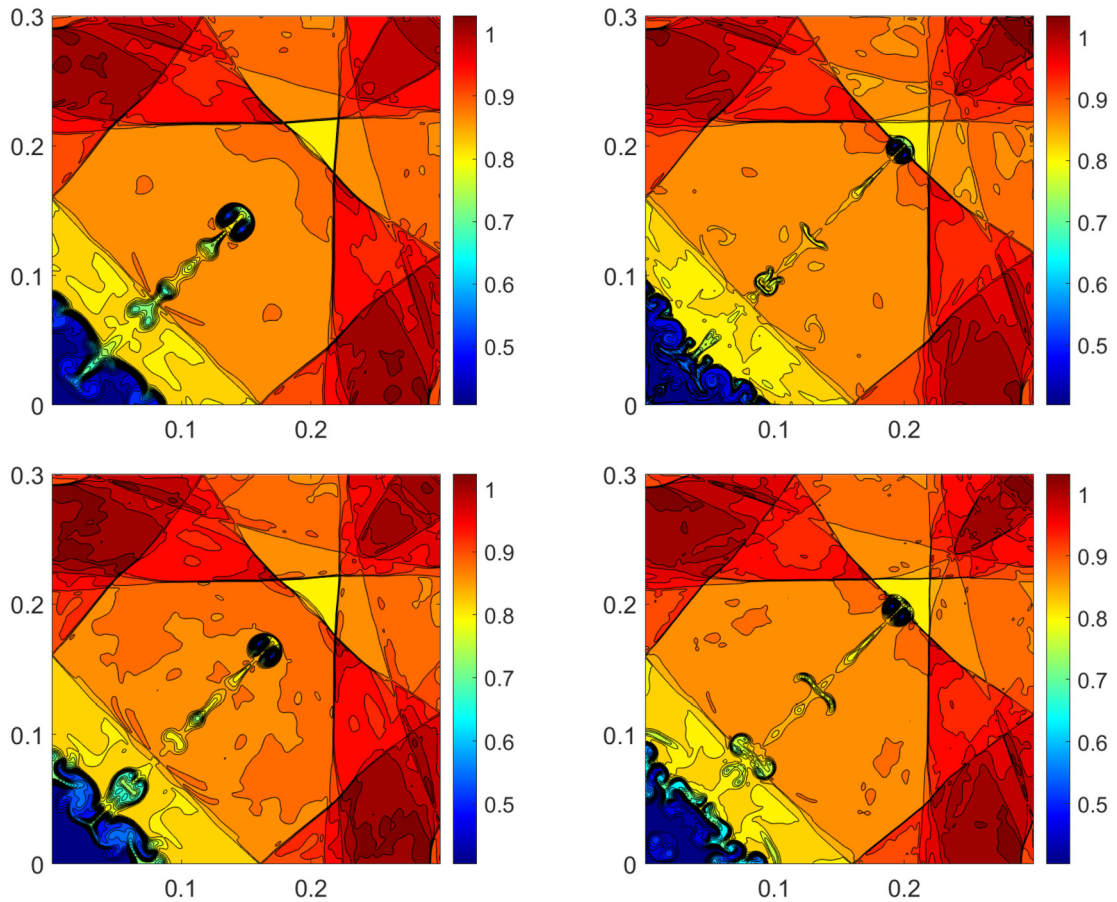


Fig. 5.8. Example 10: Density (ρ) computed by the Old CU scheme using $\Delta x = \Delta y = 1/2000$ (top left), New CU schemes using $\Delta x = \Delta y = 1/2000$ (top right), Old CU scheme using $\Delta x = \Delta y = 1/2500$ (bottom left), and Old CU scheme using $\Delta x = \Delta y = 3/10000$ (bottom right).

by the New CU scheme propagates much further in the direction of $y = x$ than the jet produced by the Old CU scheme: This is attributed to a much smaller amount of numerical dissipation present in the New CU scheme.

In this example, we also check the efficiency of the proposed LCD-based CU scheme by performing a more thorough comparison between the New and Old CU schemes: We now take into account additional computational cost of the New CU scheme. To this end, we measure the CPU time consumed during the above calculations by the New CU scheme and refine the mesh used by the Old CU scheme to the level that exactly the same CPU time is consumed to compute both of the numerical solutions. The corresponding grids are $\Delta x = \Delta y = 1/2000$ for the New CU scheme, and $\Delta x = \Delta y = 1/2500$ for the Old CU scheme (this solution is plotted in Fig. 5.8 (bottom left)). The obtained numerical results indicate that the New CU scheme still achieves a much higher resolution than the Old CU scheme.

It is instructive to check whether the solution computed by the Old CU scheme on even finer mesh will be comparable with the New CU solution. To this end, we refine the mesh to the level $\Delta x = \Delta y = 3/10000$ and plot the obtained Old CU scheme in Fig. 5.8 (bottom right). As one can see, this solution is similar to the New CU solution shown in Fig. 5.8 (top right). This shows that the New CU scheme is capable of resolving the same details on a substantially coarser grid due to the smaller amount of numerical diffusion present in the scheme.

Example 11—Kelvin-Helmholtz (KH) instability

In this example, we study the KH instability, which develops in the test problem taken from [5,6,8,17,34]. We take the following initial data:

$$(\rho(x, y, 0), u(x, y, 0)) = \begin{cases} (1, -0.5 + 0.5e^{(y+0.25)/L}), & y < -0.25, \\ (2, 0.5 - 0.5e^{(-y-0.25)/L}), & -0.25 < y < 0, \\ (2, 0.5 - 0.5e^{(y-0.25)/L}), & 0 < y < 0.25, \\ (1, -0.5 + 0.5e^{(0.25-y)/L}), & y > 0.25, \end{cases}$$

$$v(x, y, 0) = 0.01 \sin(4\pi x), \quad p(x, y, 0) \equiv 1.5,$$

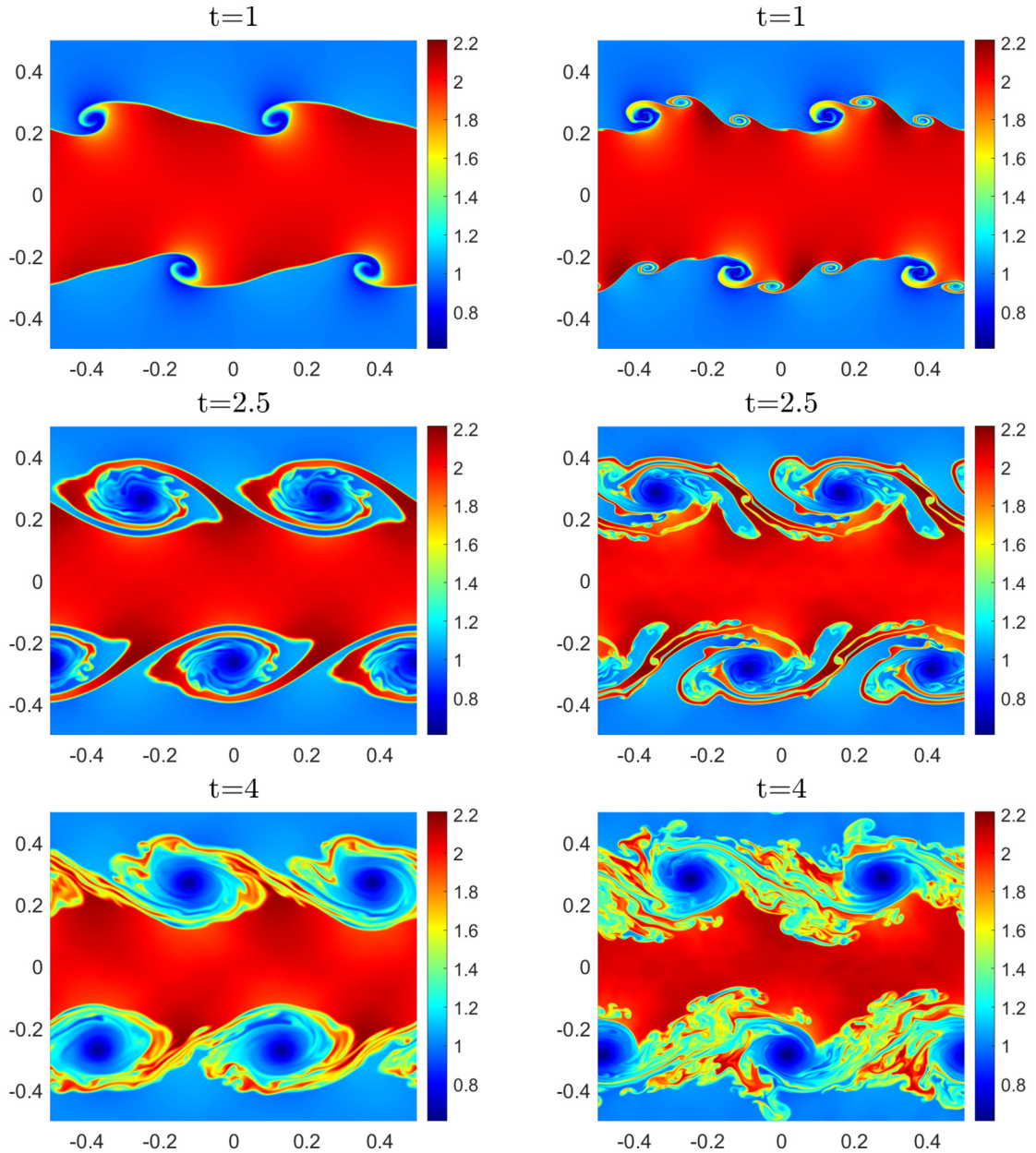


Fig. 5.9. Example 8: Time snapshots of density (ρ) computed by the Old (left column) and New (right column) CU schemes at $t = 1$ (top row), $t = 2.5$ (middle row), and $t = 4$ (bottom row).

where L is a smoothing parameter (we take $L = 0.00625$), which corresponds to a thin shear interface with a perturbed vertical velocity field v in the conducted simulations. Periodic boundary conditions are imposed on all of the four sides of the computational domain $[-0.5, 0.5] \times [-0.5, 0.5]$. We compute the numerical solutions until the final time $t = 4$ by both the New and Old CU schemes on a uniform mesh with $\Delta x = \Delta y = 1/1024$. The numerical results at times $t = 1, 2.5$, and 4 are presented in Fig. 5.9. As one can see, at the early time $t = 1$, the vortex streets formed by the adaptive scheme are more pronounced. These structures continue growing exponentially in time showing much more complicated turbulent mixing captured by the New CU scheme, especially at the final time $t = 4$. Clearly, the New CU scheme outperforms the Old one in achieving a higher resolution of the KH instabilities.

For the KH instability problem, it is well-known that numerical solutions do not converge when the mesh is refined, since the limiting solution is not a weak solution but a so-called dissipative weak solution; see [4] for more details. The latter can be approximated by the Cesàro averages computed from the numerical solutions on meshes with different resolutions. As proved in [4], the Cesàro averages converge strongly (in the L^q -norm with $1 \leq q < \infty$) to a dissipative weak solution.

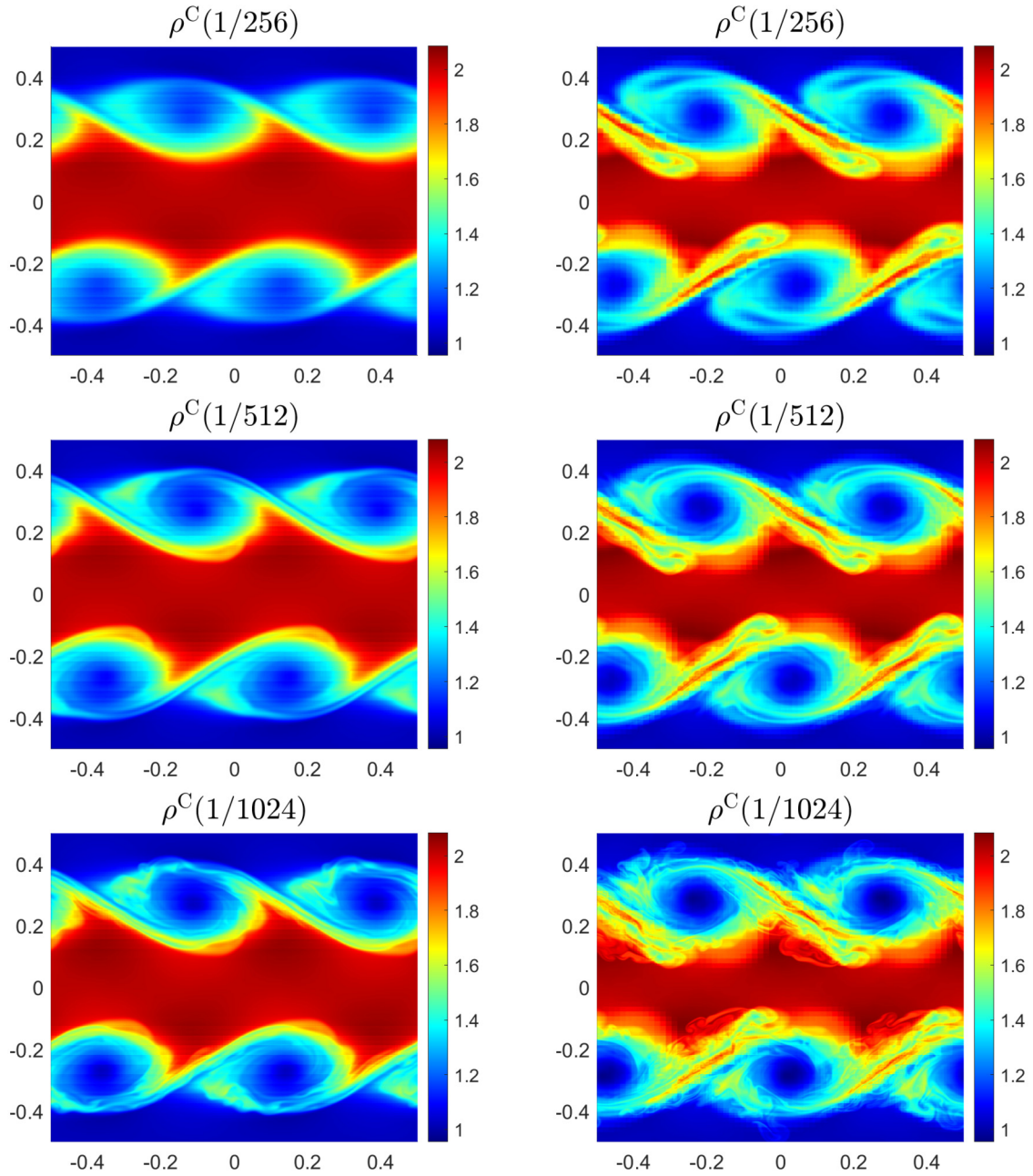


Fig. 5.10. Example 11: Cesàro averages of the density ρ^C computed by the Old (left column) and New (right column) CU schemes at $t = 4$.

In order to approximate the limiting solution, we consider the Cesàro averages of the densities computed at the final time $t = 4$ by the New and Old CU schemes. To this end, we introduce the sequence of meshes with the cells of size $1/2^n$, $n = 5, \dots, 10$, and denote by $\rho(1/2^n)$ the density computed on the corresponding mesh. We then project the obtained coarser mesh solutions with $n = 5, \dots, m - 1$ onto the finer mesh with $n = m$ (the projection is carried out using the minmod reconstruction [28,32,41] applied to the density field) and denote the obtained results still by $\rho(1/2^n)$, $n = 5, \dots, m$. After this, we compute the Cesàro averages by

$$\rho^C(1/2^m) = \frac{\rho(1/2^5) + \dots + \rho(1/2^m)}{m - 4}, \quad m = 8, 9, 10. \tag{5.1}$$

The obtained results, presented in Fig. 5.10 for both the New and Old CU schemes, indicate non-uniqueness of the limiting dissipative weak solution that apparently depends on the choice of the numerical diffusion. This leads to an interesting question on suitable selection criteria that can be studied in the future.

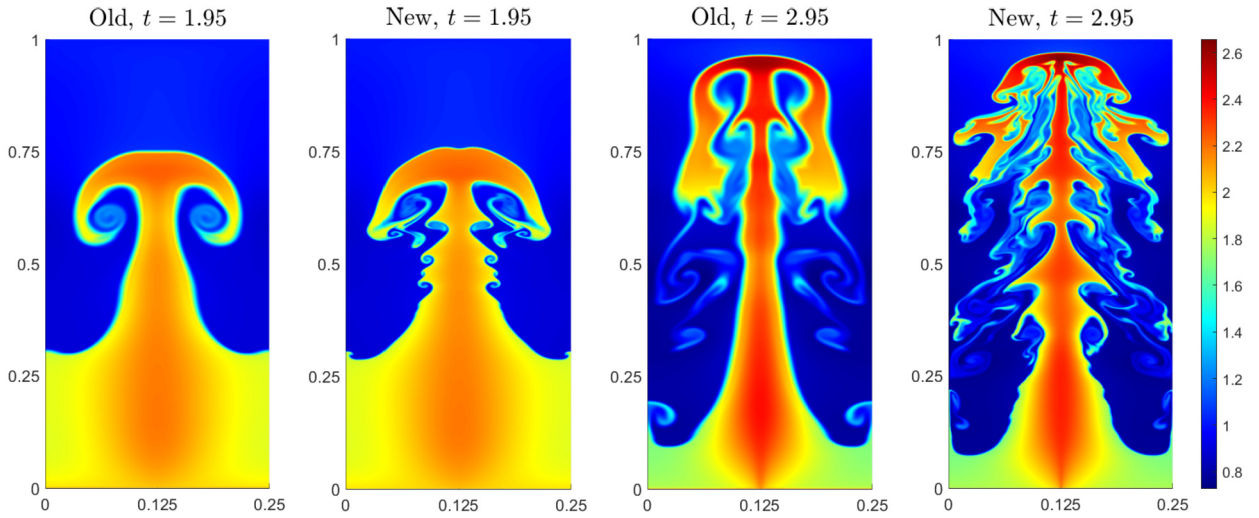


Fig. 5.11. Example 12: Density (ρ) computed by the Old and New CU schemes at different times.

Example 12—Rayleigh-Taylor (RT) instability

In the last example taken from [8,17,38,43], we investigate the RT instability, which is a physical phenomenon occurring when a layer of heavier fluid is placed on top of a layer of lighter fluid. The model is governed by the 2-D Euler equations (1.1), (C.1)–(C.2) with added gravitational source terms. In the studied setup, the gravitational force acts in the positive y -direction and the modified system reads as

$$\begin{aligned} \rho_t + (\rho u)_x + (\rho v)_y &= 0, \\ (\rho u)_t + (\rho u^2 + p)_x + (\rho uv)_y &= 0, \\ (\rho v)_t + (\rho uv)_x + (\rho v^2 + p)_y &= \rho, \\ E_t + [u(E + p)]_x + [v(E + p)]_y &= \rho v. \end{aligned}$$

This system is considered subject to the following initial conditions:

$$(\rho(x, y, 0), u(x, y, 0), v(x, y, 0), p(x, y, 0)) = \begin{cases} (2, 0, -0.025 c \cos(8\pi x), 2y + 1), & y < 0.5, \\ (1, 0, -0.025 c \cos(8\pi x), y + 1.5), & \text{otherwise,} \end{cases}$$

where $c := \sqrt{\gamma p/\rho}$ is the speed of sound, and the solid wall boundary conditions at $x = 0$ and $x = 0.25$, and the following Dirichlet boundary conditions at the top and bottom boundaries:

$$(\rho, u, v, p)|_{y=1} = (1, 0, 0, 2.5), \quad (\rho, u, v, p)|_{y=0} = (2, 0, 0, 1).$$

We compute the numerical solutions in the computational domain $[0, 0.25] \times [0, 1]$ discretized using a uniform mesh with $\Delta x = \Delta y = 1/1024$ until the final time $t = 2.95$ by both the New and Old CU schemes. The numerical results at times $t = 1.95$ and 2.95 , presented in Fig. 5.11, show a significant difference in performance of the New and Old CU schemes. Indeed, the New CU scheme is capable of capturing the RT instability with a much higher resolution of the complicated solution structure. Once again, this indicates that the New CU scheme is substantially less dissipative than its Old counterpart.

As in Example 11, we approximate the dissipative weak solution using the Cesàro averages, which are computed by (5.1) using the same sequence of meshes. The obtained results for both the New and Old CU schemes at the times $t = 1.95$ and 2.95 are presented in Figs. 5.12 and 5.13, respectively. Once again, we observe that the limiting dissipative weak solution is apparently non-unique as it seems to depend on the choice of the numerical diffusion.

CRedit authorship contribution statement

Alina Chertock: Conceptualization, Funding acquisition, Investigation, Methodology, Visualization, Writing – original draft, Writing – review & editing. **Shaoshuai Chu:** Conceptualization, Formal analysis, Investigation, Methodology, Software, Validation, Visualization, Writing – original draft, Writing – review & editing. **Michael Herty:** Conceptualization, Funding acquisition, Investigation, Methodology, Visualization, Writing – original draft, Writing – review & editing. **Alexander Kurganov:** Conceptualization, Funding acquisition, Investigation, Methodology, Project administration, Software, Supervision, Validation, Visualization, Writing – original draft, Writing – review & editing. **Mária Lukáčová-Medvid’ová:** Conceptualization, Funding acquisition, Investigation, Methodology, Visualization, Writing – original draft, Writing – review & editing.

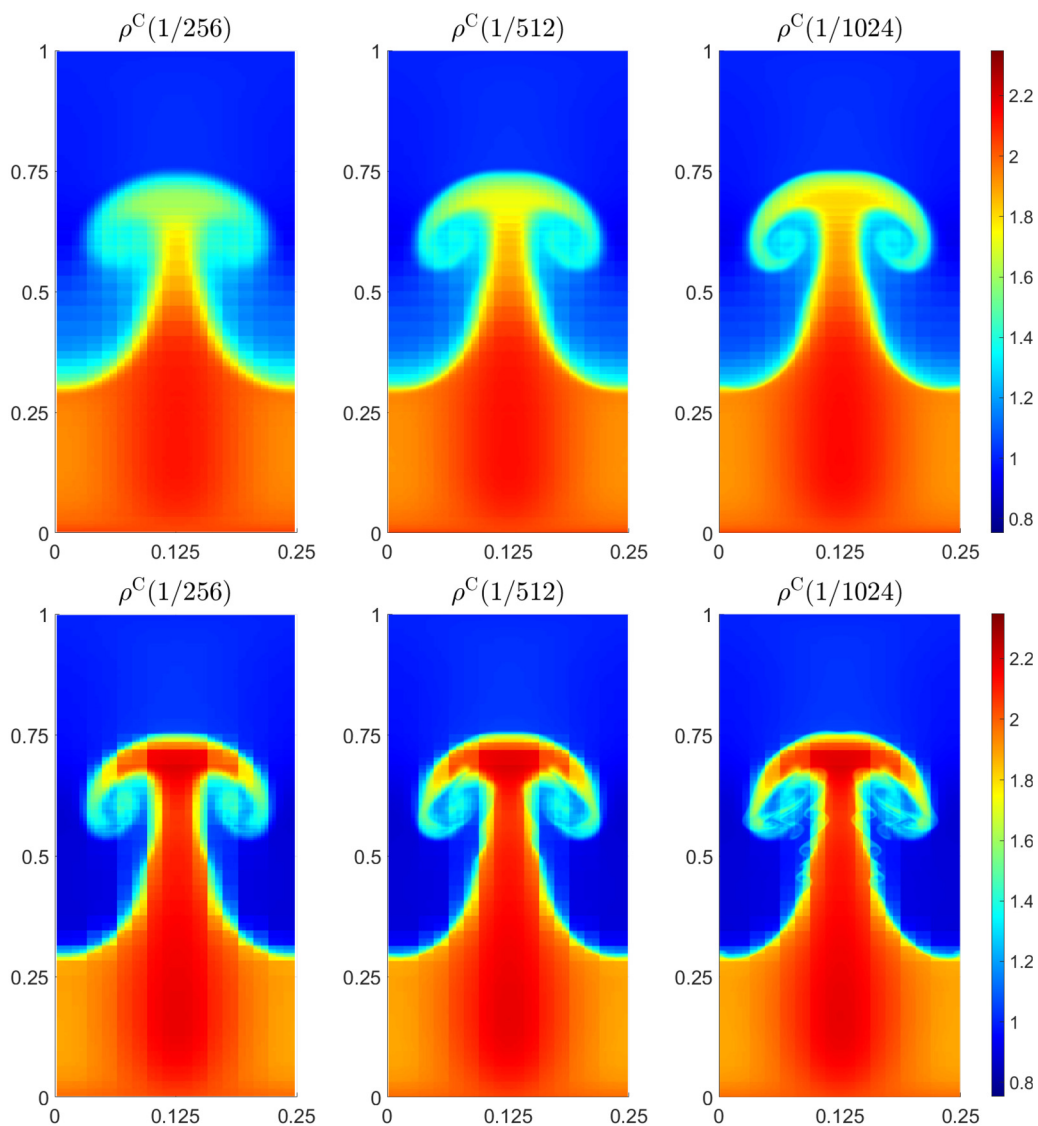


Fig. 5.12. Example 12: Cesàro averages of the density ρ^C computed by the Old (top row) and New (bottom row) CU schemes at $t = 1.95$.

Declaration of competing interest

The authors declare that they have no known competing financial interests or personal relationships that could have appeared to influence the work reported in this paper.

Data availability

Data will be made available on request.

Acknowledgement

The work of A. Chertock was supported in part by NSF grants DMS-1818684 and DMS-2208438. The work of M. Herty was supported in part by the DFG (German Research Foundation) through 20021702/GRK2326, 333849990/IRTG-2379, HE5386/18-1, 19-2, 22-1, 23-1 and under Germany's Excellence Strategy EXC-2023 Internet of Production 390621612. The work of A. Kurganov was supported in part by NSFC grants 12171226 and 12111530004, and by the fund of the Guangdong Provincial Key Laboratory of Computational Science and Material Design (No. 2019B030301001). The work of M. Lukáčová-Medvid'ová has been funded by the DFG (German Research Foundation) under the SFB/TRR 146 Multiscale

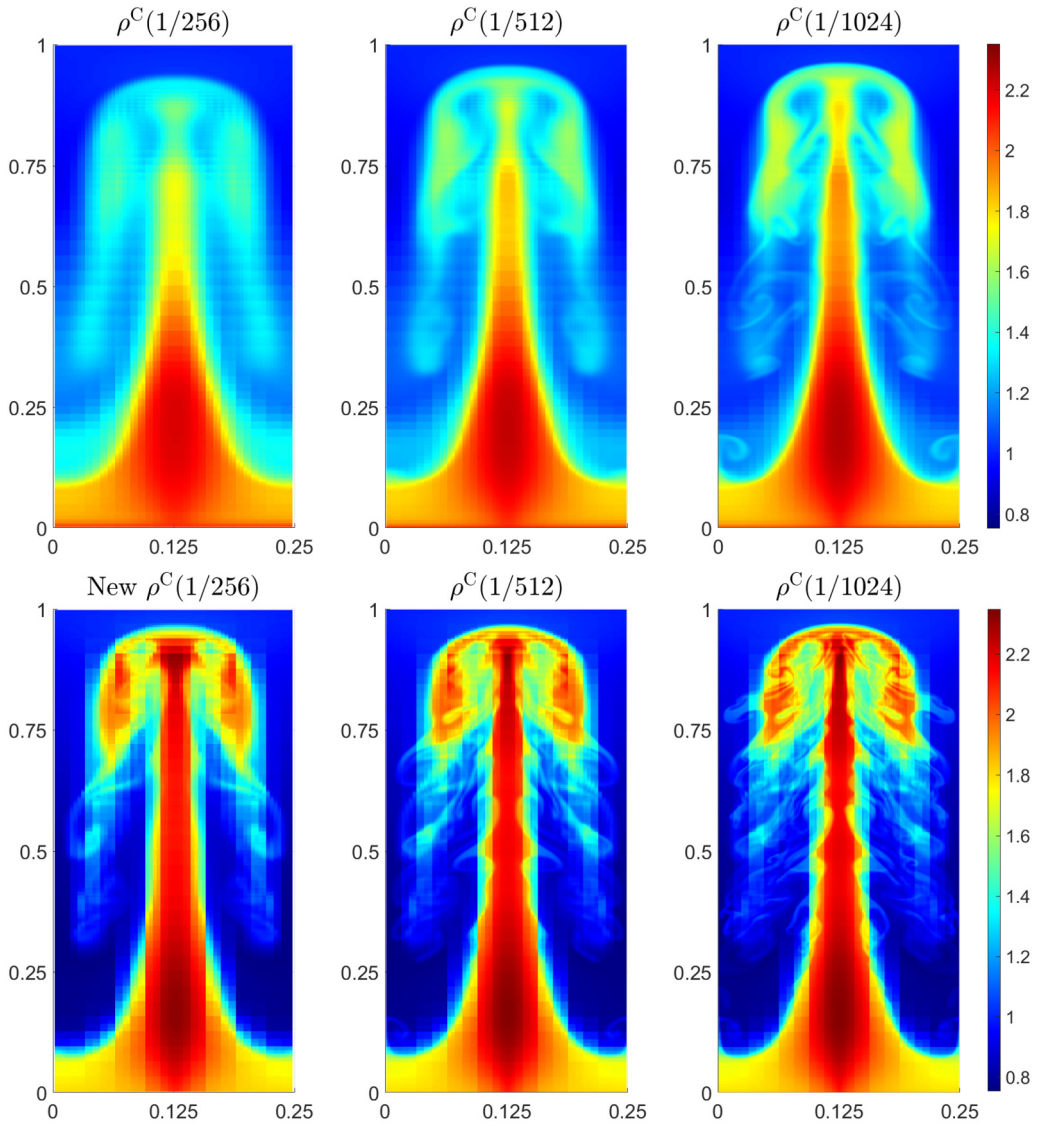


Fig. 5.13. Example 12: Same as in Fig. 5.12, but for $t = 2.95$.

Simulation Methods for Soft Matter Systems. M. Lukáčová-Medvid'ová gratefully acknowledges support of the Gutenberg Research College of University Mainz and the Mainz Institute of Multiscale Modeling.

Appendix A. LCD matrices for the 1-D Euler equations of gas dynamics

The 1-D Euler equations of gas dynamics read as the system (2.1) with

$$\mathbf{U} = \begin{pmatrix} \rho \\ \rho u \\ E \end{pmatrix} \quad \text{and} \quad \mathbf{F}(\mathbf{U}) = \begin{pmatrix} \rho u \\ \rho u^2 + p \\ u(E + p) \end{pmatrix},$$

where ρ , u , p , and E are the density, velocity, pressure and total energy, respectively. The system is completed through the following equations of state (EOS):

$$E = \rho e + \frac{1}{2} \rho u^2, \quad e = \frac{p}{(\gamma - 1)\rho}, \quad (\text{A.1})$$

where e is the specific internal energy, and γ is the parameter representing the specific heat ratio.

We first compute the Jacobian

$$A(\mathbf{U}) = \frac{\partial \mathbf{F}}{\partial \mathbf{U}}(\mathbf{U}) = \begin{pmatrix} 0 & 1 & 0 \\ \frac{\gamma-3}{2}u^2 & (3-\gamma)u & \gamma-1 \\ -\frac{\gamma u E}{\rho} + (\gamma-1)u^3 & H - (\gamma-1)u^2 & \gamma u \end{pmatrix},$$

where $H = \frac{E+p}{\rho}$ is the total specific enthalpy. We then introduce the matrices

$$\hat{A}_{j+\frac{1}{2}} = \begin{pmatrix} 0 & 1 & 0 \\ \frac{\gamma-3}{2}\hat{u}^2 & (3-\gamma)\hat{u} & \gamma-1 \\ -\frac{\gamma\hat{u}\hat{E}}{\hat{\rho}} + (\gamma-1)\hat{u}^3 & \hat{H} - (\gamma-1)\hat{u}^2 & \gamma\hat{u} \end{pmatrix},$$

where $\hat{(\cdot)}$ stands for the following averages:

$$\hat{\rho} = \frac{\bar{\rho}_j + \bar{\rho}_{j+1}}{2}, \quad \hat{u} = \frac{u_j + u_{j+1}}{2}, \quad \hat{p} = \frac{p_j + p_{j+1}}{2}, \quad \hat{H} = \frac{\hat{E} + \hat{p}}{\hat{\rho}}, \quad \hat{E} = \frac{\hat{p}}{\gamma-1} + \frac{1}{2}\hat{\rho}\hat{u}^2,$$

where

$$u_j = \frac{(\overline{\rho u})_j}{\bar{\rho}_j} \quad \text{and} \quad p_j = (\gamma-1) \left[\bar{E}_j - \frac{1}{2}\bar{\rho}_j u_j^2 \right].$$

Notice that all of the $\hat{(\cdot)}$ quantities have to have a subscript index, that is, $\hat{(\cdot)} = \hat{(\cdot)}_{j+\frac{1}{2}}$, but we omit it for the sake of brevity for all of the quantities except for \hat{A} . We then compute the matrix $R_{j+\frac{1}{2}}$ composed of the right eigenvectors of $\hat{A}_{j+\frac{1}{2}}$ and obtain

$$R_{j+\frac{1}{2}} = \begin{pmatrix} 1 & 1 & 1 \\ \hat{u} - \hat{c} & \hat{u} & \hat{u} + \hat{c} \\ \hat{H} - \hat{u}\hat{c} & \hat{u}^2 & \hat{H} + \hat{u}\hat{c} \end{pmatrix} \quad \text{and} \quad R_{j+\frac{1}{2}}^{-1} = \frac{1}{\hat{\phi}} \begin{pmatrix} \frac{\hat{u}^2}{2} + \frac{\hat{u}\hat{\phi}}{2\hat{c}} & -\hat{u} - \frac{\hat{\phi}}{2\hat{c}} & 1 \\ 2\hat{\phi} - 2\hat{H} & 2\hat{u} & -2 \\ \frac{\hat{u}^2}{2} - \frac{\hat{u}\hat{\phi}}{2\hat{c}} & -\hat{u} + \frac{\hat{\phi}}{2\hat{c}} & 1 \end{pmatrix}, \tag{A.2}$$

where $\hat{\phi} = 2\hat{H} - \hat{u}^2$ and $\hat{c} = \sqrt{\gamma\hat{p}/\hat{\rho}}$.

Appendix B. Proof of Lemma 5.1

In order to prove that the New CU scheme can maintain constant velocity and pressure, it is sufficient to show that if at a given time level t , $u_j(t) \equiv \check{u}$ and $p_j(t) \equiv \check{p}$, then

$$(\mathcal{F}_{j+\frac{1}{2}}^{\text{LCD}})^{(2)} = \check{u}(\mathcal{F}_{j+\frac{1}{2}}^{\text{LCD}})^{(1)} + \check{p} \quad \text{and} \quad (\mathcal{F}_{j+\frac{1}{2}}^{\text{LCD}})^{(3)} = \frac{\check{u}^2}{2}(\mathcal{F}_{j+\frac{1}{2}}^{\text{LCD}})^{(1)} + \frac{\gamma\check{u}\check{p}}{\gamma-1}, \tag{B.1}$$

where $(\mathcal{F}_{j+\frac{1}{2}}^{\text{LCD}})^{(i)}$ denotes the i th component of the LCD-based CU numerical flux $\mathcal{F}_{j+\frac{1}{2}}^{\text{LCD}}$ (3.6)–(3.8), (A.2). Indeed, let us for simplicity assume that the ODE system (3.5) is discretized using the forward Euler method and if (B.1) holds, we then obtain

$$\bar{\rho}_j(t + \Delta t) = \bar{\rho}_j(t) - \frac{\Delta t}{\Delta x} \left[(\mathcal{F}_{j+\frac{1}{2}}^{\text{LCD}})^{(1)} - (\mathcal{F}_{j-\frac{1}{2}}^{\text{LCD}})^{(1)} \right],$$

and hence

$$\begin{aligned} (\overline{\rho u})_j(t + \Delta t) &= (\overline{\rho u})_j(t) - \frac{\Delta t}{\Delta x} \left[(\mathcal{F}_{j+\frac{1}{2}}^{\text{LCD}})^{(2)} - (\mathcal{F}_{j-\frac{1}{2}}^{\text{LCD}})^{(2)} \right] \\ &= \bar{\rho}_j(t)\check{u} - \frac{\Delta t}{\Delta x} \check{u} \left[(\mathcal{F}_{j+\frac{1}{2}}^{\text{LCD}})^{(1)} - (\mathcal{F}_{j-\frac{1}{2}}^{\text{LCD}})^{(1)} \right] = \bar{\rho}_j(t + \Delta t)\check{u}, \end{aligned}$$

which immediately implies

$$u_j(t + \Delta t) = \frac{(\overline{\rho u})_j(t + \Delta t)}{\bar{\rho}_j(t + \Delta t)} = \check{u}. \tag{B.2}$$

We then obtain

$$\begin{aligned} \bar{E}_j(t + \Delta t) &= \bar{E}_j(t) - \frac{\Delta t}{\Delta x} \left[(\mathcal{F}_{j+\frac{1}{2}}^{\text{LCD}})^{(3)} - (\mathcal{F}_{j-\frac{1}{2}}^{\text{LCD}})^{(3)} \right] \\ &= \bar{E}_j(t) - \frac{\check{u}^2 \Delta t}{2 \Delta x} \left[(\mathcal{F}_{j+\frac{1}{2}}^{\text{LCD}})^{(1)} - (\mathcal{F}_{j-\frac{1}{2}}^{\text{LCD}})^{(1)} \right] = \bar{E}_j(t) + \frac{\check{u}^2}{2} [\bar{\rho}_j(t + \Delta t) - \bar{\rho}_j(t)]. \end{aligned}$$

Using the EOS (A.1) and (B.2), the last equation can be rewritten as

$$\frac{\bar{p}_j(t + \Delta t)}{\gamma - 1} + \frac{\check{u}^2}{2} \bar{\rho}_j(t + \Delta t) = \frac{\check{p}}{\gamma - 1} + \frac{\check{u}^2}{2} \bar{\rho}_j(t) + \frac{\check{u}^2}{2} [\bar{\rho}_j(t + \Delta t) - \bar{\rho}_j(t)],$$

which results in

$$p_j(t + \Delta t) = \check{p}. \tag{B.3}$$

A similar computation establishing (B.2) and (B.3) can be carried out for other ODE solvers.

In order to complete the proof of Lemma 5.1, we now need to verify (B.1) for the LCD-based CU numerical flux (3.6)–(3.8), (A.2). To this end, we use the notations introduced in Appendix A, the fact that $(P_i^{\text{LCD}})_{j+\frac{1}{2}} + (M_i^{\text{LCD}})_{j+\frac{1}{2}} \equiv 1$ for $i \in \{1, 2, 3\}$ and for all j (see (3.8)), and after a proper simplification arrive at

$$\begin{aligned} (\mathcal{F}_{j+\frac{1}{2}}^{\text{LCD}})^{(1)} &= \frac{1}{\hat{\phi}} \left[\left(\frac{\check{u}\check{p}}{\gamma - 1} - \frac{\hat{\phi}\check{p}}{2\hat{c}} \right) (P_1^{\text{LCD}})_{j+\frac{1}{2}} + \left(\frac{2\gamma\check{u}\check{p}}{\hat{\rho}(\gamma - 1)} \rho_{j+\frac{1}{2}}^- - \frac{2\check{u}\check{p}}{\gamma - 1} \right) (P_2^{\text{LCD}})_{j+\frac{1}{2}} \right. \\ &\quad + \left(\frac{\check{u}\check{p}}{\gamma - 1} + \frac{\hat{\phi}\check{p}}{2\hat{c}} \right) (P_3^{\text{LCD}})_{j+\frac{1}{2}} + \left(\frac{\check{u}\check{p}}{\gamma - 1} - \frac{\hat{\phi}\check{p}}{2\hat{c}} \right) (M_1^{\text{LCD}})_{j+\frac{1}{2}} \\ &\quad + \left(\frac{2\gamma\check{u}\check{p}}{\hat{\rho}(\gamma - 1)} \rho_{j+\frac{1}{2}}^+ - \frac{2\check{u}\check{p}}{\gamma - 1} \right) (M_2^{\text{LCD}})_{j+\frac{1}{2}} + \left(\frac{\check{u}\check{p}}{\gamma - 1} + \frac{\hat{\phi}\check{p}}{2\hat{c}} \right) (M_3^{\text{LCD}})_{j+\frac{1}{2}} \\ &\quad \left. + \frac{2\gamma\check{p}}{\hat{\rho}(\gamma - 1)} (Q_2^{\text{LCD}})_{j+\frac{1}{2}} (\rho_{j+\frac{1}{2}}^+ - \rho_{j+\frac{1}{2}}^-) \right], \\ (\mathcal{F}_{j+\frac{1}{2}}^{\text{LCD}})^{(2)} &= \check{u} (\mathcal{F}_{j+\frac{1}{2}}^{\text{LCD}})^{(1)} + \frac{\check{p}}{\hat{\phi}} \left[\left(\frac{\hat{\phi}}{2} - \frac{\hat{c}\check{u}}{\gamma - 1} \right) (P_1^{\text{LCD}})_{j+\frac{1}{2}} + \left(\frac{\hat{\phi}}{2} + \frac{\hat{c}\check{u}}{\gamma - 1} \right) (P_3^{\text{LCD}})_{j+\frac{1}{2}} \right. \\ &\quad \left. + \left(\frac{\hat{\phi}}{2} - \frac{\hat{c}\check{u}}{\gamma - 1} \right) (M_1^{\text{LCD}})_{j+\frac{1}{2}} + \left(\frac{\hat{\phi}}{2} + \frac{\hat{c}\check{u}}{\gamma - 1} \right) (M_3^{\text{LCD}})_{j+\frac{1}{2}} \right] = \check{u} (\mathcal{F}_{j+\frac{1}{2}}^{\text{LCD}})^{(1)} + \check{p}, \\ (\mathcal{F}_{j+\frac{1}{2}}^{\text{LCD}})^{(3)} &= \frac{\check{u}^2}{2} (\mathcal{F}_{j+\frac{1}{2}}^{\text{LCD}})^{(1)} + \frac{\check{p}}{\hat{\phi}} \left[\left(\frac{\gamma\check{u}\check{p}}{\hat{\rho}(\gamma - 1)^2} - \frac{\hat{c}\check{u}^2}{\gamma - 1} + \frac{\hat{\phi}}{2}\check{u} - \frac{\gamma\hat{\phi}\check{p}}{2\hat{c}\hat{\rho}(\gamma - 1)} \right) (P_1^{\text{LCD}})_{j+\frac{1}{2}} \right. \\ &\quad + \left(\frac{\gamma\check{u}\check{p}}{\hat{\rho}(\gamma - 1)^2} + \frac{\hat{c}\check{u}^2}{\gamma - 1} + \frac{\hat{\phi}}{2}\check{u} + \frac{\gamma\hat{\phi}\check{p}}{2\hat{c}\hat{\rho}(\gamma - 1)} \right) (P_3^{\text{LCD}})_{j+\frac{1}{2}} \\ &\quad + \left(\frac{\gamma\check{u}\check{p}}{\hat{\rho}(\gamma - 1)^2} - \frac{\hat{c}\check{u}^2}{\gamma - 1} + \frac{\hat{\phi}}{2}\check{u} - \frac{\gamma\hat{\phi}\check{p}}{2\hat{c}\hat{\rho}(\gamma - 1)} \right) (M_1^{\text{LCD}})_{j+\frac{1}{2}} \\ &\quad \left. + \left(\frac{\gamma\check{u}\check{p}}{\hat{\rho}(\gamma - 1)^2} + \frac{\hat{c}\check{u}^2}{\gamma - 1} + \frac{\hat{\phi}}{2}\check{u} + \frac{\gamma\hat{\phi}\check{p}}{2\hat{c}\hat{\rho}(\gamma - 1)} \right) (M_3^{\text{LCD}})_{j+\frac{1}{2}} \right] = \frac{\check{u}^2}{2} (\mathcal{F}_{j+\frac{1}{2}}^{\text{LCD}})^{(1)} + \frac{\gamma\check{u}\check{p}}{\gamma - 1}. \end{aligned}$$

It should be observed that the last equality has been established using the formula $\hat{\phi} = \frac{2\gamma\check{p}}{\hat{\rho}(\gamma - 1)}$, which can be obtained from the definitions of $\hat{\phi}$, \hat{H} , and \hat{E} . \square

Appendix C. LCD-based piecewise linear reconstruction for the 2-D Euler equations of gas dynamics

The 2-D Euler equations of gas dynamics read as (1.1) with

$$\mathbf{U} = \begin{pmatrix} \rho \\ \rho u \\ \rho v \\ E \end{pmatrix}, \quad \mathbf{F}(\mathbf{U}) = \begin{pmatrix} \rho u \\ \rho u^2 + p \\ \rho uv \\ u(E + p) \end{pmatrix}, \quad \text{and} \quad \mathbf{G}(\mathbf{U}) = \begin{pmatrix} \rho v \\ \rho uv \\ \rho v^2 + p \\ v(E + p) \end{pmatrix}, \tag{C.1}$$

where ρ is the density, u and v are the x - and y -velocities, p is the pressure, and E is the total energy. The system is completed through the following EOS:

$$E = \rho e + \frac{\rho}{2}(u^2 + v^2), \quad e = \frac{p}{(\gamma - 1)\rho}, \tag{C.2}$$

where, as in the 1-D case, e is the specific internal energy, and γ is the parameter representing the specific heat ratio.

In what follows, we discuss the reconstruction of the point values $\mathbf{U}_{j,k}^{E,W}$ and $\mathbf{\Gamma}_{j,k}^{E,W}$ (the point values $\mathbf{U}_{j,k}^{N,S}$ and $\mathbf{\Gamma}_{j,k}^{N,S}$ can be computed in a similar manner and we omit the details for the sake of brevity). To this end, we first compute the Jacobian

$$A(\mathbf{U}) = \frac{\partial \mathbf{F}}{\partial \mathbf{U}}(\mathbf{U}) = \begin{pmatrix} 0 & 1 & 0 & 0 \\ \frac{\gamma - 3}{2}u^2 + \frac{\gamma - 1}{2}v^2 & (3 - \gamma)u & (1 - \gamma)v & \gamma - 1 \\ -uv & v & u & 0 \\ -\frac{\gamma u E}{\rho} + (\gamma - 1)u(u^2 + v^2) & H - (\gamma - 1)u^2 & (1 - \gamma)uv & \gamma u \end{pmatrix},$$

where, as in the 1-D case, $H = \frac{E+p}{\rho}$. We then introduce the matrices

$$\widehat{A}_{j+\frac{1}{2},k} = \begin{pmatrix} 0 & 1 & 0 & 0 \\ \frac{\gamma - 3}{2}\hat{u}^2 + \frac{\gamma - 1}{2}\hat{v}^2 & (3 - \gamma)\hat{u} & (1 - \gamma)\hat{v} & \gamma - 1 \\ -\hat{u}\hat{v} & \hat{v} & \hat{u} & 0 \\ -\frac{\gamma \hat{u} \hat{E}}{\hat{\rho}} + (\gamma - 1)\hat{u}(\hat{u}^2 + \hat{v}^2) & \hat{H} - (\gamma - 1)\hat{u}^2 & (1 - \gamma)\hat{u}\hat{v} & \gamma \hat{u} \end{pmatrix},$$

where $(\hat{\cdot})$ stands for the following averages:

$$\hat{\rho} = \frac{\bar{\rho}_{j,k} + \bar{\rho}_{j+1,k}}{2}, \quad \hat{u} = \frac{u_{j,k} + u_{j+1,k}}{2}, \quad \hat{v} = \frac{v_{j,k} + v_{j+1,k}}{2}, \quad \hat{p} = \frac{p_{j,k} + p_{j+1,k}}{2},$$

$$\hat{H} = \frac{\hat{E} + \hat{p}}{\hat{\rho}}, \quad \hat{E} = \frac{\hat{p}}{\gamma - 1} + \frac{\hat{\rho}}{2}(\hat{u}^2 + \hat{v}^2),$$

where

$$u_{j,k} = \frac{(\overline{\rho u})_{j,k}}{\bar{\rho}_{j,k}}, \quad v_{j,k} = \frac{(\overline{\rho v})_{j,k}}{\bar{\rho}_{j,k}}, \quad \text{and} \quad p_{j,k} = (\gamma - 1) \left[\bar{E}_{j,k} - \frac{\rho_{j,k}}{2} (u_{j,k}^2 + v_{j,k}^2) \right].$$

As in Appendix A, all of the $(\hat{\cdot})$ quantities have to have a subscript index, that is, $(\hat{\cdot}) = (\hat{\cdot})_{j+\frac{1}{2},k}$, which we omit for the sake of brevity for all of the quantities except for \widehat{A} . We then compute the matrix $R_{j+\frac{1}{2},k}$ composed of the right eigenvectors of $\widehat{A}_{j+\frac{1}{2},k}$ and obtain

$$R_{j+\frac{1}{2},k} = \begin{pmatrix} 1 & 1 & 0 & 1 \\ \hat{u} - \hat{c} & \hat{u} & 0 & \hat{u} + \hat{c} \\ \hat{v} & \hat{v} & 1 & \hat{v} \\ \hat{H} - \hat{u}\hat{c} & \frac{\hat{u}^2 + \hat{v}^2}{2} & \hat{v} & \hat{H} + \hat{u}\hat{c} \end{pmatrix}$$

and

$$R_{j+\frac{1}{2},k}^{-1} = \frac{1}{\hat{\phi}} \begin{pmatrix} \frac{\hat{u}^2 + \hat{v}^2}{2} + \frac{\hat{u}\hat{\phi}}{2\hat{c}} & -\hat{u} - \frac{\hat{\phi}}{2\hat{c}} & -\hat{v} & 1 \\ 2\hat{\phi} - 2\hat{H} & 2\hat{u} & 2\hat{v} & -2 \\ -\hat{v}\hat{\phi} & 0 & \hat{\phi} & 0 \\ \frac{\hat{u}^2 + \hat{v}^2}{2} - \frac{\hat{u}\hat{\phi}}{2\hat{c}} & -\hat{u} + \frac{\hat{\phi}}{2\hat{c}} & -\hat{v} & 1 \end{pmatrix},$$

where $\hat{\phi} = 2\hat{H} - \hat{u}^2 - \hat{v}^2$ and $\hat{c} = \sqrt{\gamma \hat{p} / \hat{\rho}}$.

We then introduce the local characteristic variables in the neighborhood of $(x, y) = (x_{j+\frac{1}{2}}, y_k)$:

$$\mathbf{\Gamma}_{\ell,k} = R_{j+\frac{1}{2},k}^{-1} \bar{\mathbf{U}}_{\ell,k}, \quad \ell = j - 1, \dots, j + 2.$$

Equipped with the values $\mathbf{\Gamma}_{j-1,k}$, $\mathbf{\Gamma}_{j,k}$, $\mathbf{\Gamma}_{j+1,k}$, and $\mathbf{\Gamma}_{j+2,k}$, we compute

$$(\mathbf{\Gamma}_x)_{j,k} = \text{minmod} \left(2 \frac{\mathbf{\Gamma}_{j,k} - \mathbf{\Gamma}_{j-1,k}}{\Delta x}, \frac{\mathbf{\Gamma}_{j+1,k} - \mathbf{\Gamma}_{j-1,k}}{2\Delta x}, 2 \frac{\mathbf{\Gamma}_{j+1,k} - \mathbf{\Gamma}_{j,k}}{\Delta x} \right),$$

and

$$(\Gamma_x)_{j+1,k} = \text{minmod} \left(2 \frac{\Gamma_{j+1,k} - \Gamma_{j,k}}{\Delta x}, \frac{\Gamma_{j+2,k} - \Gamma_{j,k}}{2\Delta x}, 2 \frac{\Gamma_{j+2,k} - \Gamma_{j+1,k}}{\Delta x} \right),$$

where the minmod function, defined in (2.7), is applied in the component-wise manner. We then use these slopes to evaluate

$$\Gamma_{j,k}^E = \Gamma_{j,k} + \frac{\Delta x}{2} (\Gamma_x)_{j,k} \quad \text{and} \quad \Gamma_{j+1,k}^W = \Gamma_{j+1,k} - \frac{\Delta x}{2} (\Gamma_x)_{j+1,k},$$

and finally obtain the corresponding point values of \mathbf{U} by

$$\mathbf{U}_{j+\frac{1}{2}}^{E,W} = R_{j+\frac{1}{2},k} \Gamma_{j+\frac{1}{2},k}^{E,W}.$$

References

- [1] P. Arminjon, M.C. Viallon, Généralisation du schéma de Nessyahu-Tadmor pour une équation hyperbolique à deux dimensions d'espace, *C. R. Acad. Sci. Paris Sér. I Math.* 320 (1995) 85–88.
- [2] M. Ben-Artzi, J. Falcovitz, Generalized Riemann Problems in Computational Fluid Dynamics, Cambridge Monographs on Applied and Computational Mathematics, vol. 11, Cambridge University Press, Cambridge, 2003.
- [3] W.S. Don, D.-M. Li, Z. Gao, B.-S. Wang, A characteristic-wise alternative WENO-Z finite difference scheme for solving the compressible multicomponent non-reactive flows in the overestimated quasi-conservative form, *J. Sci. Comput.* 82 (2020), 27.
- [4] E. Feireisl, M. Lukáčová-Medvid'ová, H. Mizerová, B. She, Numerical Analysis of Compressible Fluid Flows, MS&A. Modeling, Simulation and Applications, vol. 20, Springer, Cham, 2021.
- [5] E. Feireisl, M. Lukáčová-Medvid'ová, B. She, Y. Wang, Computing oscillatory solutions of the Euler system via \mathcal{K} -convergence, *Math. Models Methods Appl. Sci.* 31 (2021) 537–576.
- [6] U. Fjordholm, S. Mishra, E. Tadmor, On the computation of measure-valued solutions, *Acta Numer.* 25 (2016) 567–679.
- [7] K.O. Friedrichs, Symmetric hyperbolic linear differential equations, *Commun. Pure Appl. Math.* 7 (1954) 345–392.
- [8] N.K. Garg, A. Kurganov, Y. Liu, Semi-discrete central-upwind Rankine-Hugoniot schemes for hyperbolic systems of conservation laws, *J. Comput. Phys.* 428 (2021) 110078.
- [9] S.K. Godunov, A difference method for numerical calculation of discontinuous solutions of the equations of hydrodynamics, *Mat. Sb.* 47 (1959) 271–306.
- [10] S. Gottlieb, D. Ketcheson, C.-W. Shu, Strong Stability Preserving Runge-Kutta and Multistep Time Discretizations, World Scientific Publishing Co. Pte. Ltd., Hackensack, NJ, 2011.
- [11] S. Gottlieb, C.-W. Shu, E. Tadmor, Strong stability-preserving high-order time discretization methods, *SIAM Rev.* 43 (2001) 89–112.
- [12] J.S. Hesthaven, Numerical Methods for Conservation Laws: From Analysis to Algorithms, *Comput. Sci. Eng.*, vol. 18, SIAM, Philadelphia, 2018.
- [13] G.S. Jiang, E. Tadmor, Nonoscillatory central schemes for multidimensional hyperbolic conservation laws, *SIAM J. Sci. Comput.* 19 (1998) 1892–1917.
- [14] Y. Jiang, C.-W. Shu, M. Zhang, An alternative formulation of finite difference weighted ENO schemes with Lax-Wendroff time discretization for conservation laws, *SIAM J. Sci. Comput.* 35 (2013) A1137–A1160.
- [15] E. Johnsen, On the treatment of contact discontinuities using WENO schemes, *J. Comput. Phys.* 230 (2011) 8665–8668.
- [16] D.I. Ketcheson, R.J. LeVeque, M.J. del Razo, Riemann Problems and Jupyter Solutions, Fundamentals of Algorithms, vol. 16, Society for Industrial and Applied Mathematics (SIAM), Philadelphia, PA, 2020.
- [17] A. Kurganov, Y. Liu, Y. Zeitlin, Numerical dissipation switch for two-dimensional central-upwind schemes, *ESAIM: Math. Model. Numer. Anal.* 55 (2021) 713–734.
- [18] A. Kurganov, P. Noelle, G. Petrova, Semidiscrete central-upwind schemes for hyperbolic conservation laws and Hamilton-Jacobi equations, *SIAM J. Sci. Comput.* 23 (2001) 713–734.
- [19] A. Kurganov, M. Prugger, T. Wu, Second-order fully discrete central-upwind scheme for two-dimensional hyperbolic systems of conservation laws, *SIAM J. Sci. Comput.* 39 (2017) A947–A965.
- [20] A. Kurganov, C.-T. Lin, On the reduction of numerical dissipation in central-upwind schemes, *Commun. Comput. Phys.* 2 (2007) 141–163.
- [21] A. Kurganov, E. Tadmor, New high-resolution semi-discrete central schemes for Hamilton-Jacobi equations, *J. Comput. Phys.* 160 (2000) 720–742.
- [22] A. Kurganov, E. Tadmor, Solution of two-dimensional Riemann problems for gas dynamics without Riemann problem solvers, *Numer. Methods Partial Differ. Equ.* 18 (2002) 584–608.
- [23] A. Kurganov, R. Xin, Central-upwind schemes and contact discontinuities. Application to the Euler equations of gas dynamics, Submitted. Preprint available at <https://sites.google.com/view/alexander-kurganov/publications>.
- [24] P.D. Lax, Weak solutions of nonlinear hyperbolic equations and their numerical computation, *Commun. Pure Appl. Math.* 7 (1954) 159–193.
- [25] R.J. LeVeque, Finite Volume Methods for Hyperbolic Problems, Cambridge Texts in Appl. Math., Cambridge University Press, Cambridge, UK, 2002.
- [26] D. Levy, G. Puppo, G. Russo, Central WENO schemes for hyperbolic systems of conservation laws, *Math. Model. Numer. Anal.* 33 (1999) 547–571.
- [27] K.-A. Lie, S. Noelle, An improved quadrature rule for the flux-computation in staggered central difference schemes in multidimensions, *J. Sci. Comput.* 18 (2003) 69–81.
- [28] K.-A. Lie, S. Noelle, On the artificial compression method for second-order nonoscillatory central difference schemes for systems of conservation laws, *SIAM J. Sci. Comput.* 24 (2003) 1157–1174.
- [29] R. Liska, B. Wendroff, Comparison of several difference schemes on 1D and 2D test problems for the Euler equations, *SIAM J. Sci. Comput.* 25 (2003) 995–1017.
- [30] H. Liu, A numerical study of the performance of alternative weighted ENO methods based on various numerical fluxes for conservation law, *Appl. Math. Comput.* 296 (2017) 182–197.
- [31] X.D. Liu, E. Tadmor, Third order nonoscillatory central scheme for hyperbolic conservation laws, *Numer. Math.* 79 (1998) 397–425.
- [32] H. Nessyahu, E. Tadmor, Nonoscillatory central differencing for hyperbolic conservation laws, *J. Comput. Phys.* 87 (1990) 408–463.
- [33] T. Nonomura, K. Fujii, Characteristic finite-difference WENO scheme for multicomponent compressible fluid analysis: overestimated quasi-conservative formulation maintaining equilibriums of velocity, pressure, and temperature, *J. Comput. Phys.* 340 (2017) 358–388.
- [34] J. Panuelos, J. Wadsley, N. Kevlahan, Low shear diffusion central schemes for particle methods, *J. Comput. Phys.* 414 (2020) 109454.
- [35] J. Qiu, C.-W. Shu, On the construction, comparison, and local characteristic decomposition for high-order central WENO schemes, *J. Comput. Phys.* 183 (2002) 187–209.
- [36] C.W. Schulz-Rinne, Classification of the Riemann problem for two-dimensional gas dynamics, *SIAM J. Math. Anal.* 24 (1993) 76–88.

- [37] C.W. Schulz-Rinne, J.P. Collins, H.M. Glaz, Numerical solution of the Riemann problem for two-dimensional gas dynamics, *SIAM J. Sci. Comput.* 14 (1993) 1394–1394.
- [38] J. Shi, Y.-T. Zhang, C.-W. Shu, Resolution of high order WENO schemes for complicated flow structures, *J. Comput. Phys.* 186 (2003) 690–696.
- [39] C.-W. Shu, Essentially non-oscillatory and weighted essentially non-oscillatory schemes, *Acta Numer.* 5 (2020) 701–762.
- [40] C.-W. Shu, S. Osher, Efficient implementation of essentially non-oscillatory shock-capturing schemes, *J. Comput. Phys.* 77 (1988) 439–471.
- [41] P.K. Sweby, High resolution schemes using flux limiters for hyperbolic conservation laws, *SIAM J. Numer. Anal.* 21 (1984) 995–1011.
- [42] E.F. Toro, *Riemann Solvers and Numerical Methods for Fluid Dynamics: A Practical Introduction*, third ed., Springer-Verlag, Berlin, Heidelberg, 2009.
- [43] B.-S. Wang, W.S. Don, N.K. Garg, A. Kurganov, Fifth-order A-WENO finite-difference schemes based on a new adaptive diffusion central numerical flux, *SIAM J. Sci. Comput.* 42 (2020) A3932–A3956.
- [44] B.-S. Wang, P. Li, Z. Gao, W.S. Don, An improved fifth order alternative WENO-Z finite difference scheme for hyperbolic conservation laws, *J. Comput. Phys.* 374 (2018) 469–477.
- [45] P. Woodward, P. Colella, The numerical solution of two-dimensional fluid flow with strong shocks, *J. Comput. Phys.* 54 (1988) 115–173.
- [46] Y. Zheng, *Systems of Conservation Laws. Two-Dimensional Riemann Problems*, Progress in Nonlinear Differential Equations and Their Applications, Birkhäuser Boston, Inc., Boston, MA, 2001.